Mass Transfer in Coal Seams for CO_2 Sequestration

F. Y. Wang, Z. H. Zhu, P. Massarotto, and V. Rudolph
Division of Chemical Engineering, School of Engineering, The University of Queensland, Brisbane, Qld. 4072, Australia

DOI 10.1002/aic.11115
Published online February 27, 2007 in Wiley InterScience (www.interscience.wiley.com).

CO_2 sequestration in coal seams is a relatively new technique to simultaneously achieve enhanced coal bed methane production and reduced CO_2 emission. In this article, we integrate understandings in individual research fields to provide improved insight into the nature of this complex process. Our current overall model constructed from a number of sub-models consists of mass transfer in four pore types, namely, fractures, micro-, meso-, and macro-pores, all having pore size dependent characteristics. Key parameters are estimated using well established methods from the general literature. Three mechanisms of coal swelling leading to permeability variations during adsorption are proposed based on molecular simulations. The macroscopic level model is validated using a true tri-axial stress coal permeameter, which provides previously unpublished, accurate dynamic measurements of systems properties in three orthogonal directions including changes to the coal matrix volume. The integrated model provides a more complete and flexible representation for this complex system. © 2007 American Institute of Chemical Engineers *AIChE J,* 53: 1028–1049, 2007
Keywords: complex fluids, diffusion (microporous), mathematical modeling, porous media, simulation, process

Introduction

CO_2 sequestration in coal seams is a relatively new technique to simultaneously achieve enhanced coal bed methane (ECBM) production and reduced CO_2 emission. The significance and current status of this research area have been comprehensively reviewed in two recent review papers.[1,2] In any particular practical case feasibility, economics, and risk evaluation require the determination of a number of operational conditions. Both theoretical analysis and experimental investigation are essential for the development of effective ECBM strategies. A multidisciplinary approach is required, covering a number of challenging scientific areas such as multi-component transport in porous media, coal characterization, geophysics, and geochemistry. In spite of an extensive recent literature in relevant areas, significant gaps in knowledge can still be identified because of the complexity and broad scientific coverage of the field, which are identified as follows.

1. The multiscale nature, which ranges from molecular interactions in the length scale of nanometers and time scale of micro seconds all the way to coal seam operations with lengths of kilometers and performance analyzed in hours, days, and even weeks. Significant research advances have been achieved in both microscopic level using molecular simulations, and macroscopic level studies through commercialized software packages, for coal bed methane (CBM) simulations. However, coupling these two scales remains elusive as evidenced by the fact that the recent conceptual advances achieved from fundamental studies are scarcely incorporated into the large scale simulators. For example, it can be shown that neglecting micro-pore size distributions in CBM models leads to considerable errors. It is necessary to develop adequate transition procedures to bridge the micro- and macro-scale formulations.
2. A process can be described by many models with different complexity and accuracy. We adopt the position of Box and Draper[3] that: "Essentially, all models are wrong,

Correspondence concerning this article should be addressed to F. Y. Wang at f.wang@eng.uq.edu.au.

but some are useful." They also emphasized that: "... the practical question is how wrong do they have to be to not be useful." A model could be useful for a particular application, but may fail for other purposes. A study on model hierarchy could be an effective strategy for model form selections based on applications. Unfortunately, no systematic study on the hierarchical modeling of ECBM processes has been reported in the literature. Guidelines for model form selections for specified end-uses are yet to be developed.

3. A significant number of modeling papers have relied on the experimental data reported by other researchers for model validation and parameter estimation. Because of the complexity of coal characteristics, and possible inconsistency between experimental and simulation conditions, the validation and estimation results may not be reliable. It is highly desirable to integrate the theoretical study, numerical simulations, and experimental investigations into a unified research program.
4. Numerical values of important coal parameters reported in some articles have lost their original physical significance even though outcomes with acceptable accuracies were obtained.[4,5] For example, both pore and surface diffusivities estimated in these articles, e.g. by back-fitting, are many orders smaller than values computed in fundamental studies. There are two main reasons for the dramatic deviations between different estimation methods: (1) model structures cannot adequately represent the real physical systems, leading to the error accumulation in the estimated parameters; and (2) estimation methods based on macroscopic measurements are insufficient for the unique determination of multiple parameters associated with different mechanisms. The effective pore and surface diffusivities estimated using the overall measurement data have been called "pseudo diffusivities" by Yang.[6] Modified modeling strategies should incorporate computations based on the fundamental theory where appropriate, and be able to provide convincing physical explanations about discrepancies.
5. Although adsorption induced dimensional changes (swelling and shrinkage) have been investigated extensively,[7,8] the dynamic evolution of coal structures in CO_2 sequestration processes have not been comprehensively studied. An important consequence of coal swelling/shrinkage during sorption processes is the permeability change, which has attracted a considerable amount of research effort. However, models developed for the prediction of this phenomenon normally assume constant geophysical properties, such as constant volumetric swelling coefficient and Young's modulus, and negligible effects on adsorption and diffusion processes. There is strong evidence to show that geophysical properties of coal change dynamically and nonlinearly. For example, with increasing gas adsorbed the smaller the volumetric swelling coefficient, and the larger the Young's modulus of fracture. Consequently, some key parameters must be identified dynamically. This involves dynamic optimization, which has not been reported previously.

There are two popular dynamic modeling strategies for the representation of transport phenomena in porous media, namely, the pore network approach and the particulate approach. In the particulate approach, macro-spheres are produced through the aggregation of micro-spheres of uniform size. These macro-spheres are then packed in the sample cell for the diffusion-adsorption studies. Since the system provides dual porosity and diffusivity, the model is named the bi-disperse model. This technique was originally developed for spherical catalysts and adsorbents with quite restrictive mathematical assumptions, including negligible pressure gradient and isotropic properties of the adsorbents.[6] It has been extended to coal technology in recent years.[4,5,9] Because of the limitations of the bi-disperse model, described by Yang,[6] and the complexity of coal structures, its extension to coal technology has led to the loss of physical significance of several key parameters, such as pore and surface diffusivities. The reported pore network approach reviewed by Tsotsis et al.[1] involves transport through the macro-pore and cleat fracture networks, diffusion through the meso-pore and micro-pore regions of the coal matrix, adsorption of CO_2 onto, and de-sorption of CH_4 from the surface of the micropores. That is, macro-pore cleat fractures and the coal matrix itself represent separate classes of transport paths in the sense that each has its own distinct characteristics. In spite of the scientific advances and practical significance of the two-path pore network approach,[10] it can be demonstrated through numerical simulations that the mass transfer mechanisms in each path are much more complicated than that incorporated in the conventional models. For example, there is no justification for the assumptions regarding negligible diffusive mass transfer in macro-pores, and convective mass transfer in meso-pores used in the development of the conventional models. Furthermore, there are four experimentally distinguishable pore types in coals that have a role in dynamic structural changes associated with the pressurized adsorption/de-sorption processes. The lumping of macro-pores with cleats leads to significant model errors. These issues should be adequately addressed in modeling studies.

There are advantages and disadvantages associated with both strategies. A comparative study between two approaches will certainly lead to valuable insights. Methods to relax the restrictive assumptions imposed on the particulate approach to broaden its application areas is also an important research topic. These may include the development of three dimensional particulate models and studies on multisized particle packing.

This article attempts to fill partly some of these gaps in knowledge through the development of an integrated modeling approach to the dynamics of mass transfer in porous media with particular applications to CO_2 sequestration in coal seams. The process under study can be depicted by a spectrum of representations ranging between a very simple black-box model based on input-output data only, and a highly complex mechanistic model consisting of a large scale partial differential equation (PDE) system with parameters estimated through molecular simulations. Intermediate models, denoted as grey-box models, may be developed between these two extremes to form a hierarchical tree. The selection of model forms depends on the requirements of applications. It is impractical to develop a pure mechanistic model because of incomplete knowledge in a variety of relevant fields. In this article, emphasis is placed on the development of an upper-intermediate class model based on some physical

understanding of the process. Our modeling strategy covers the following areas.

1. Develop an overall model structure incorporating convective flow in cleats associated with aperture and permeability computations, convective and diffusive flows in macro- and meso-pores, adsorption/de-sorption and surface diffusion in micro-pores. Micro-pore size distribution and pore network correlations are incorporated into the overall model.
2. Estimate key parameters using thermodynamic relationships, molecular simulations, and reliable correlations. On-line identification techniques using measurement data are only used for the estimation of a minimum number of parameters, which cannot be directly or independently measured, or computed from theory.
3. Validate the macroscopic level model using a true tri-axial stress coal permeameter (TTSCP), which provides accurate dynamic measurements of gas flow-rates, compositions, dimensional variations of specimens, temperatures, and pressures in three orthogonal directions.
4. Study the mechanisms of coal swelling, leading to dynamic permeability changes during adsorption, through molecular simulations, which quantitatively show the adsorption induced bond size and pore aperture extensions.
5. Investigate the effects of pore size distributions on fluid flow and adsorption behavior. This is particularly important for the mass transfer in micro-pores.

In this article, the Stefan-Maxwell analysis[11] and computations of viscous flow[12] are applied to the fluid phase inside meso and macro-pores[13] within the dusty-gas modeling framework. In recent years, studies on Stefan-Maxwell equations for the adsorption and diffusion of pure components and binary mixtures in zeolites and carbon nanotubes have been carried out using molecular dynamics (MD) simulations with promising results.[14,15] The limitations of the reported applications of Stefan-Maxwell analysis to the micro-pore mass transfer are identified as: (1) The materials under study consist of well defined micro-pore structures with thoroughly characterized surface roughness; and (2) Studies have been restricted to pure components and binary mixtures. Because of the complexity of the coal structures, the first limitation becomes a real hurdle for the extension of the reported MD simulations to coal research. This implies that the validity of Stefan-Maxwell analysis applied to multicomponent surface diffusion in micro-pores within the coal matrix is yet to be justified. We adopt the technique suggested by Wang and Do[16] based on the concept of hypothetical concentration to address the surface diffusion for multi-component systems. The pore networks for meso-pores are characterized by using the EMT–SFA procedure. The pore size distributions in micro- and meso-pores are incorporated into the mathematical models and computer algorithms to replace the conventionally used methods based on mean pore sizes. The adsorption and desorption kinetics are investigated using experimental data obtained in our laboratories with new representations in the matrix format ready for the development of compact computer codes based on matrix operations. The physical properties are computed dynamically within the integrated computational algorithm.

Compared with the models reported in the literature, the newly developed model possesses the following advantages.

1. The integrated model consisting of four pore types with six fluxes along each axis is more complete than conventional dual or triple porosity models typically dealing with three fluxes.
2. The model is more general because of the elimination of several restrictive assumptions used in the development of current conventional models. The eliminated assumptions include the negligible pressure drop, isotropic, and homogeneous conditions for the development of bi-disperse models,[6] single mass flux, and unique pore size in each pore type for the development of both bi-disperse and pore network models.[1,6]
3. The model is more flexible because of dynamic computation of key model parameters using validated methods. These include gas phase diffusivities and viscosities, and the permeability of cleat, macro-, and meso-pores.

The shortcomings of the integrated model developed in this work can be identified as follows.

1. It is difficult to measure directly the surface diffusivities, micro-pore size distribution, pore-size dependent adsorption energies, and concentrations in the coal matrix with consistent results.
2. The overall algorithm involves the solution of partial differential-integral equations with symbolic differentiation operations, which is more complicated than the numerical schemes for solving the conventional models. Furthermore, numerical oscillations induced by step changes in boundary conditions, known as the Gibbs phenomenon, need to be accommodated.
3. Since deep coal seams are often below the water table, the single phase fluid flow addressed in this article needs to be extended to include water flow to provide a more general result for ECBM operations.

Because of the complexity of ECBM operations, a staged development of a model is inevitable to make the problem tractable. The model and framework outlined here permits incorporation of scientific advances or additional complexity, as these become available.

Experimental Equipment and Procedure

Experimental equipment

A high pressure, true tri-axial stress coal permeameter (TTSCP) is installed at The University of Queensland. The normal maximum operating pore pressure in TTSCP is 14 MPa, which replicates underground conditions up to about 1400 m depth. At 14 MPa, CO_2 is in supercritical condition. However, many prospective coal seams suitable for CO_2 sequestration are much shallower than 1400 m, allowing operations at pressures well below the CO_2 supercritical point. As a prelude to further studies on mixed phase and supercritical CO_2 flows, we report here normal single phase gas flow under pressures of 400–5000 kPa (much lower than the equipment limit). In most practical situations the ground temperature is likely to be above the CO_2 critical temperature (about 31°C) and the normal condition will be as a vapor. Nevertheless, we anticipate extension to more general models dealing with multiphase and/or supercritical fluid flows. The generalized process flow diagram of the TTSCP is schematically shown in Figure 1. A variety of fluids may be made to flow through a cubic coal sample under controlled pressure conditions, while the specimen is subject to three independ-

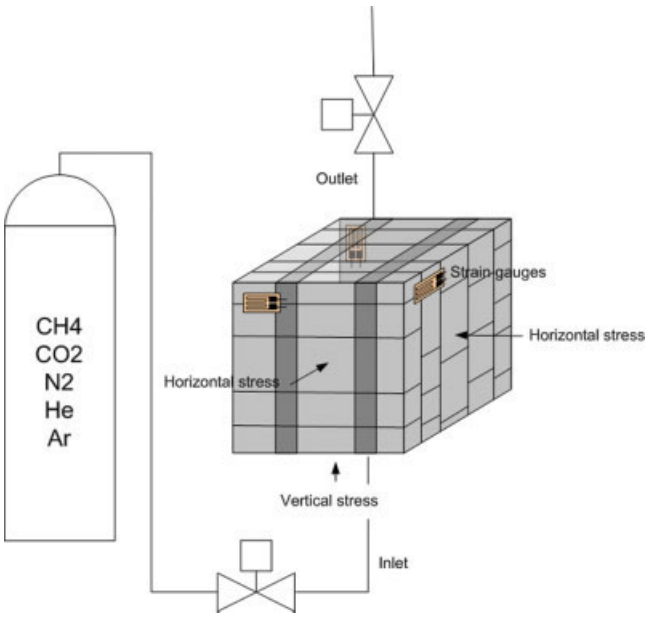

Figure 1. TTSCP.

[Color figure can be viewed in the online issue, which is available at www.interscience.wiley.com.]

ently-set, mutually-orthogonal external compressive stresses. A variety of coal specimen sizes can be accommodated up to the maximum size of 200 mm side length cube. The coal specimen size for most of the measurements is 80 mm cube. The three dimensional strain changes under operational conditions are measured using the strain gauges imbedded in the coal specimen. Details of the design features and measurement techniques are available elsewhere.[17]

Experimental procedure

A typical experimental set consists of three steps, namely setting up a standard initial condition, in which He flows through the sample for an extended flushing period, replacement of He by CH_4, and CO_2 sequestration. The complete procedure is schematically depicted in Figure 2. Upon returning to Step 1 after Step 3, the coal specimen can be reused for another set of experiments.

The transient data include flow-rates, pressures, and temperatures for inlet and outlet gas streams, outlet gas concentrations, three dimensional external stresses on the coal specimen, and the three dimensional strains. Exit gas concentrations are measured using a gas phase chromatograph. Three strain gauges are imbedded in the coal specimen for the determination of strains in three orthogonal directions. The dynamic data are recorded every 2 min by the computer data acquisition system for offline analysis.

Coal specimen preparation and surface characterization

The coal specimen preparation consists of coal specimen extraction from the coal seam, surface characterization, mercury porosimetry, and helium pycnometry analyses on small sub-samples, specimen cutting to the desired sizes, and surface polishing. These procedures are described in detail by Massarotto.[17] The most frequently tested specimen size in our laboratory is 80 mm cube, which is used in the simulation studies. This 80 mm specimen size provides a convenient compromise between what is large enough to be representative and what is practically available. Typically 40 mm cubes can be cut from standard cores and 80 mm cubes can be cut from special large cores (which generally require special, expensive drilling). We have also tested a small number of 200 mm cubes, but these need to be individually mined and present significant logistical problems in handling, transport, and cutting. For a 200 mm cube, cut in a specific orientation, a very much larger original block is required. Smaller size samples, e.g. 40 mm, are easier to handle, but show a much higher degree of heterogeneity between samples.

As an illustrative study on coal permeability, the permeability of an 80 mm cube was first measured in the TTSCP with the result of 5.3 mD. This was then cut into eight 40 mm daughters and the permeability of each of these measured. The surface features and the measured permeability of these sub-cubes are shown in Figures 3a, b. The following 10 cleat characteristics can be obtained from the subspecimens shown in Figures 3a, b:

1. Cleat frequency (density);
2. Cleat spacing distribution;
3. Cleat aperture distribution;
4. Cleat orientation/truncation;
5. Cleat length and height;
6. Cleat continuity;
7. Cleat connectivity;
8. Cleat filling (with minerals and clay);
9. Cleat tortuosity;
10. Cleat damage in sample preparation processes.

The significance of these characteristics can be analyzed as follows using Figure 3. The sub-cube F2 with the highest permeability (5.0 mD) had high cleat density, connectivity, continuity, large cleat apertures, and low tortuosity. Although the cleat density for the sub-cube F3 with the second highest

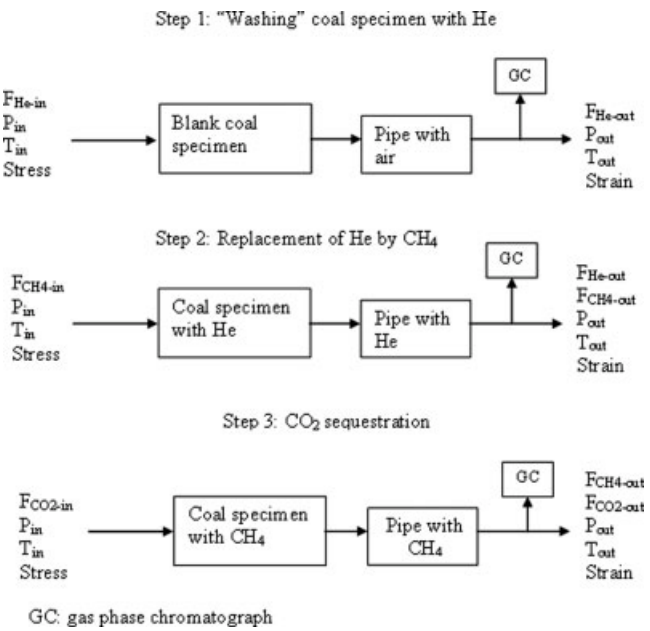

Figure 2. Experimental procedure.

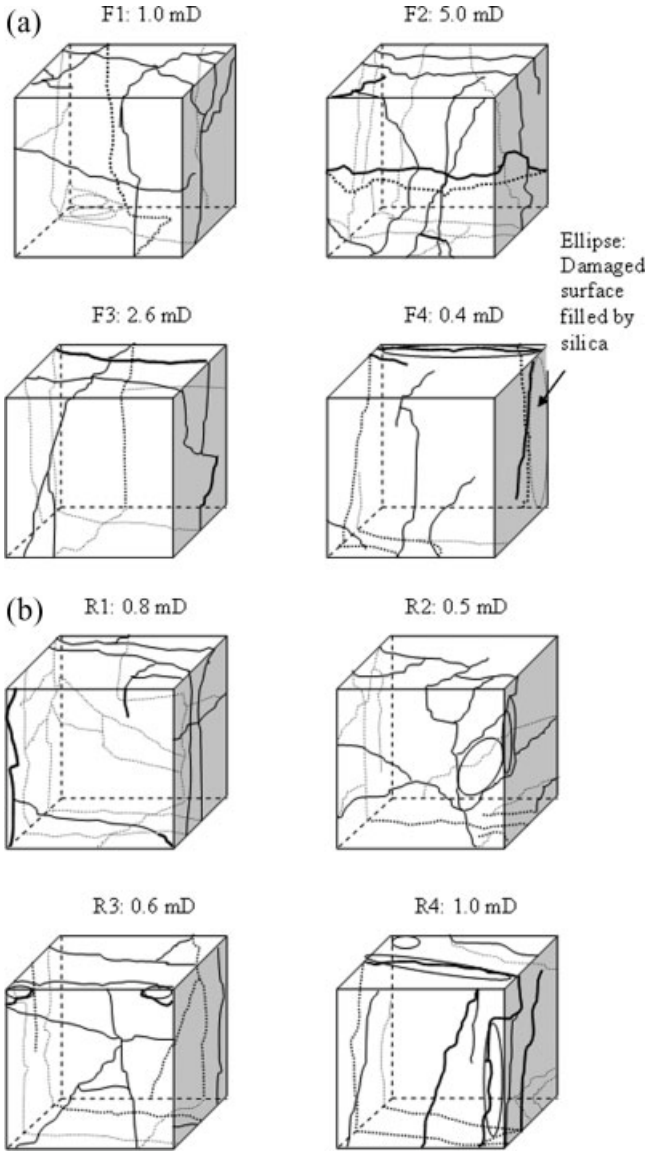

Figure 3. (a) Front four elements in the 80 mm cube coal specimen; (b) rear four elements in the 80 mm cube coal specimen.

permeability (2.6 mD) is low, the connectivity, and continuity for both face and butt cleats are high, leading to the effective use of all cleat spaces. One main cleat in sub-cube F4 was filled with silica because a part of the sample fell off during the polishing process and was then glued back. Small sections of the corners or edges on some sub-cubes required repair after cutting, indicated in Figure 3. The continuity and connectivity of the remaining cleats in this sub-cube are very low and this leads to the lowest permeability (0.4 mD). The effects of cleat orientation (truncation) on the coal permeability can be clearly demonstrated using sub-cubes R1 and R2 with relatively low permeability (0.8 and 0.5 mD respectively). A number of angular cleats in these two sub-cubes became unavailable for vertical fluid flow because they dead-end against the sides of the specimen holder. The bottle-neck effect can be seen in sub-cube R3 with low permeability (0.6 mD), in which several cleats were contracted into a single point on the surface. Sub-cube R4 should possess higher permeability than the measured value (1.0 mD) because of large cleat apertures, low tortuosity, and reasonable values of cleat density and connectivity. We believe this lower than expected permeability was caused by technical problems in the data acquisition system, providing a not entirely reliable data set. Because the larger sample has significantly less cleat damage, truncation induced cleat discontinuity and disconnections, and boundary effects; the mother specimen should possess higher permeability than the individual subspecimens. Although seven out of eight sub-cubes possess much lower permeability than the overall permeability, it can be semi-quantitatively shown that if the effects of cleat damage are removed, and the original continuity and connectivity are recovered, it is reasonable that the permeability of the assembly of the eight sub-cubes reaches the value of 5.3 mD.

Adsorption energy and pore characterization

Adsorption Energy. Adsorption energies for gases adsorbed on various porous media are normally computed using the Lennard–Jones potential energy equation or its modified formats, such as the Steele equation.[18] Figure 4 shows the adsorption energy in slit pores with different widths using the Steele 10-4-3 potential energy equation, which is described in Appendix A. The significance of adsorption energy computations for coal specimens includes the determination of the parameters in adsorption isotherms and the estimation of surface diffusivities which will be explained later.

The adsorption energies of N_2 and CH_4 depicted in Figure 4 are very close to that reported by Cui et al.,[9] except for the CO_2 profile, which is significantly higher than they reported (although the same potential energy equation was used). Importantly, for micro-pores in the range of $0.36 < w < 0.46$ nm the adsorption energy of CO_2 is always larger than that of CH_4. Our laboratory measurements using density functional theory (DFT) indicate that a significant amount of micro-pores do lie in this range. Also, the difference between adsorption energies of CO_2 and CH_4 shown in is Figure 4 is

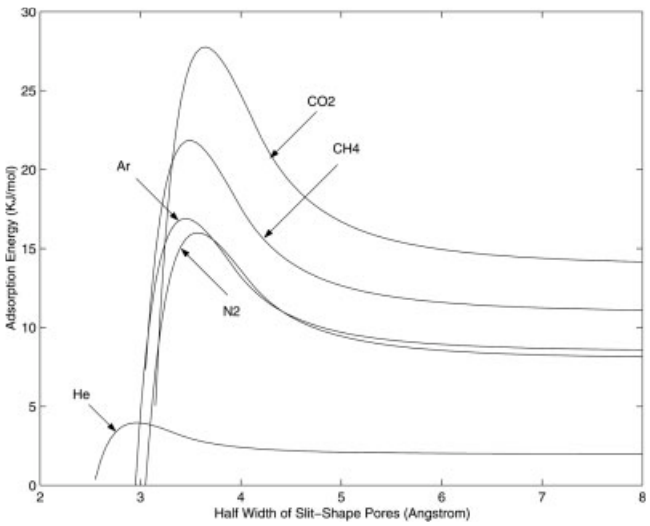

Figure 4. Adsorption energy in slit shape micro-pores.

much larger than that reported by Cui et al.,[9] who we believe may have presented underestimated values.

Pore Size Distributions. Porosity in coal is composed of micro-pores (5–20 Å), meso-pores (20–500 Å, macro-pores (500Å–0.1 μm), and cleats (0.1 μm–2 mm). The size range of cleats is very broad. The mean cleat aperture in the unstressed coal specimen shown in Figure 3 is estimated as 110 μm, which is slightly higher than the most frequently measured cleat size range of 0.1–50 μm reported by Gamson et al.[19] (suspected stressed samples). Since the Young's modulus of the cleat is much smaller than that of coal matrix, the cleat aperture reduces rapidly with increased external stress. Consequently, the coal specimen used in the current study represents the general situation reasonably well. A comprehensive literature review carried out by Massarotto[17] presents some commonly accepted coal data from the open literature. Generally, the data reported by Levine[20] and Gamson et al.[19] are well regarded by other researchers. The relevant points are summarized as follows. The total porosity of a coal is a strong and nonlinear function of the rank of coal measured by carbon content. It may vary from 4 to 18%. For high rank coals, the total porosity could be in the range of 4–8%. We adopt the following ratios for various pore types: cleats: 1–5%, macro-pores: 10–15%, meso-pores: 5%, and micro-pores: 70–80% of total pore volume.

Pore size distributions for meso-pores in a number of coal specimens have been measured in our laboratory. The distributions vary significantly for different coal specimens. However, the curve shapes of the distribution densities match lognormal distributions well. Consequently, we use lognormal distribution for meso-pores. The general representation of the lognormal distribution with suitable parameter values are explained in Appendix B.

There are no commonly accepted techniques for the accurate determination of micro-pore size distributions. A number of methods have been tested in our laboratory for micro-pore characterizations. The micro-pore size distributions can be represented by lognormal or Γ-distributions based on the available measurement data. The general representation of a Γ-distribution with suitable parameter values are also explained in Appendix B. It must be pointed out that the development of reliable experimental techniques for the determination of micro-pore size distributions is a very important, yet underdeveloped research area, requiring urgent research attention.

Conventional modeling strategy in coal research using averaged pore size could be acceptable for large pores, but lead to significant errors in small pores. This can be analyzed as follows. Since Knudsen diffusion, which is strongly affected by the pore size, is the dominant mass transfer mechanism in meso-pores, accurate computational results cannot be obtained without taking size distribution into account. Figure 4 shows that adsorption energies change considerably with minor variations of pore widths in the half-pore size range from 3 to 5 Å. However, a significant amount of micro-pores are in this sensitive size range as estimated by Eqs. A2 and A3. The necessity for the study regarding micro-pore size distribution will be further justified in the Results and Discussion section. Macro-pores and cleats where adsorption and Knudsen diffusion are negligible can be characterized using the averaged pore sizes in the model development with acceptably small error.

Pore Network Models. In this study, we adopt the pore network approach to the fluid dynamics in coal specimens. There are different definitions for the porosities. For example, the porosity can be defined either based on the total sample volume or based on the remaining volume, which is the total sample volume minus the summation of larger pore volumes. The first definition is popular in the coal literature, whereas the second definition could be better suited to pore network computations. To make the definitions consistent with the majority of the publications in the porous media literature, we adopt the following strategies:

(a) Separate cleats from other three pore types;
(b) Combine micro-pores with solid materials,[21] and
(c) Exclude larger pore volumes in the determination of the porosity of smaller pores.

Consequently, the total porosity does not include the cleat- and micro-porosity, leading to the following definition:

$$\varepsilon_t = \varepsilon_{ma} + \varepsilon_{me\_c} = \varepsilon_{ma} + (1 - \varepsilon_{ma})\varepsilon_{me}$$
$$\varepsilon_{me\_c} = (1 - \varepsilon_{ma})\varepsilon_{me} \quad (1)$$

where ε_t, ε_{ma}, and ε_{me} stand for total, macro-, and meso-pore porosities, respectively with the total porosity consisting of macro- and meso-porosities only; ε_{me_c} is the alternative definition of meso-pore porosity adopted in the coal literature. The advantage to combine micro-pores with solid materials is as follows. Three key parameters for micro-pores, namely porosity ε_{mi}, tortuosity τ_{mi} and surface diffusivity $D_{p\mu}$, can neither be computed rigorously nor measured directly, and therefore require online identification. If the micro-pores and solid materials are treated together, these three parameters are combined together defining a composite surface diffusivity D_μ represented by $D_\mu = (\varepsilon_{mi}\, D_{p\mu})/\tau_{mi}$, significantly simplifying the parameter identification problem. Probably, as measurement techniques advance, micro-pores and solids can be treated separately in the future providing improved accuracy and physical understanding. Archie's law is used to estimate the tortuosities of both macro- and meso-pores[22]:

$$\frac{\varepsilon}{\tau} = \varepsilon^\alpha \quad (2)$$

where α is the parameter to be determined experimentally. The range of α estimated by Sahimi[22] is from 1.3 to 4. For an activated carbon sample with the porosity $\varepsilon_{ma} = \varepsilon_{me} = 0.31$ and measured tortuosity[23] $\tau_{ma} = 4.70$, the computed α is 2.32. Because of the small coal porosities, this value of α leads to very large totuosity values for macro- and meso-pores. It seems that α for coals is in the lower part of the value range suggested by Sahimi.[22] For example, if we assume that the range of α is from 1.3 to 2, the range of macro-pore tortuosity is from 4 to 100, which seems plausible. A default value of $\alpha = 1.4$ is used for both macro- and meso-pores as the starting point of our simulations.

Since micro-pores are combined with solid materials, the computation of the micro-pore tortuosity can be avoided. The detailed modeling strategy will be described in next section. The Effective Medium Theory coupled with the smooth field approximation (EMT–SFA procedure) is employed to address mass transfer in meso-pore networks.

Development of integrated modeling framework

A simplified diagram of an element in the coal specimen is shown in Figure 5. There are six mass fluxes in the coal specimens. These are: convective fluid flow through cleats (Flux 1), bulk diffusions in macro and meso-pores (Fluxes 2 and 3), viscous flows in macro and meso-pores (Fluxes 4 and 5), and surface diffusion within microspores (Flux 6). A multiple one-dimensional modeling strategy is developed in this work for notational and computational simplicity. It can be easily extended to multidimensional systems. We use the orthogonal collocation on finite element (OCFE) method to solve the model equations numerically. In the model development, we mainly demonstrate the derivations of the governing equations in the z-direction, and use averaged properties along the x-axis. However, in the study of mass transfer between coal matrix and face cleats, concentration gradients in the x-direction are taken into account. It will be shown that the strategy of the combination of multiple one-dimensional models is more accurate than the pure one-dimensional models but much simpler than the real multi-dimensional models.

The following eight assumptions are made for the model development:

1. The fluid phase and the adsorbed phase are in local equilibrium with each other at any time in the coal matrix; however, fluid phase in cleats is not in equilibrium with the adsorbed phase.
2. The effective medium theory coupled with the smooth field approximation (EMT–SFA procedure) is an acceptable approximation for the investigation of transport phenomena in pore networks for meso-pores.[24,25]
3. The real gas law using the compression factor is applicable to the fluid phase.
4. A slit pore structure is assumed for all the pore types. However, certain analogies between slit and cylindrical pores are also assumed in order to use the well-established pore network models.
5. A pore size distribution for meso-pores is assumed as log-normal, and that for micro-pores is assumed as either log-normal or Γ-distribution.
6. A uniform pore length is assumed in the EMT-SFA procedure.
7. The system is isothermal, but extendable to non-isothermal operations.
8. Water flow is neglected at this stage.

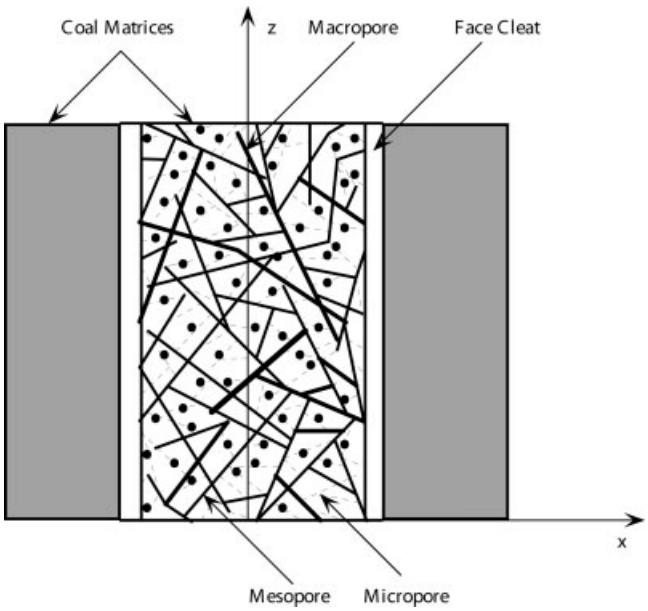

Figure 5. Element in coal specimen.

It should be pointed out that some of the assumptions could be relaxed. For example, Assumption (1) can be eliminated by the computation of the mass transfer rate between the fluid phase and the adsorbed phase,[16] Assumption (2) can be replaced by more advanced characterization techniques described by Sahimi[22] and Adler[26] for the determination of Knudson diffusivities and permeability parameters in macro- and meso-pores, and Assumption (5) can be modified by using real measurement data. In fact, the generalized algorithm for numerical simulations is developed in such a way that the users are able to select proper pre-documented functions based on particular applications. Because of the difficulties encountered in the determination of some parameters and functions, the more advanced techniques have not been widely applied to coal systems. These parameters and functions mainly include the mass transfer coefficients between the fluid phase and the adsorbed phase, pore network geometry, and connectivity, pore length distribution, and micropore size distribution. It can be seen that at this stage, the bottleneck for the relaxation of the listed assumptions is the lack of reliable measurement techniques rather than mathematical difficulties. The assumption of negligible water flow leads to significant errors for the prediction of mass transfer in coal seams below the water table. However, it makes the problem more tractable and forms a theoretical and computational foundation for further studies on multiphase fluid flow.

Fluid Flow in Cleats (Flux 1). Gilman and Beckie[10] developed a mass balance model for flow in cleats by imposing five assumptions. Two out of five assumptions are impractical for CO_2 sequestration processes. They are: [A1] Methane is the only moving substance in the coal seam (single component system is assumed); and [A4] Methane behaves like an ideal gas and its viscosity does not depend on pressure. These two assumptions are removed in this article. The multicomponent fluid flow equation in matrix form is given by:

$$\frac{\partial(\varepsilon_f \mathbf{C}_f)}{\partial t} = -\frac{\partial(\varepsilon_f V \mathbf{C}_f)}{\partial z} + \mathbf{m}(z,t)$$

$$\mathbf{C}_f = \begin{bmatrix} C_{f\_1} \\ \vdots \\ C_{f\_NC} \end{bmatrix}$$

$$\mathbf{m} = \begin{bmatrix} m_1 \\ \vdots \\ m_{NC} \end{bmatrix} \tag{3}$$

where ε_f is the fracture (cleat) porosity, $\mathbf{C}_f$ the vector of concentrations, $\mathbf{C}_{f\_i}$ the concentration of the i-th component, $i = 1, \ldots, NC$, NC the total number of components, $\mathbf{m}$ the vector of the blocks-to-fracture mass cross flow rate, m_i the

blocks-to-fracture mass cross flow rate for the i-th component, which could be either positive or negative, V the gas velocity. Equation 3 can be converted into the partial pressure representation as:

$$\frac{\partial(\varepsilon_{\mathrm{f}}\mathbf{P}_{\mathrm{f}})}{\partial t} = -\frac{\partial(\varepsilon_{\mathrm{f}}V\mathbf{P}_{\mathrm{f}})}{\partial z} + Z_{\mathrm{m}}RT\mathbf{m}(z,t)$$
$$\mathbf{P}_{\mathrm{f}} = \begin{bmatrix} P_{\mathrm{f\_1}} \\ \vdots \\ P_{\mathrm{f\_NC}} \end{bmatrix} \tag{4}$$

where $\mathbf{P}_{\mathrm{f}}$ is the vector of partial pressures in fractures, P_{f_i} is the partial pressure for the species i, and Z_{m} is the compression factor of the gas mixture. The total pressure is the summation of the partial pressures given by:

$$\frac{\partial(\varepsilon_{\mathrm{f}}P_{\mathrm{f}})}{\partial t} = -\frac{\partial(\varepsilon_{\mathrm{f}}VP_{\mathrm{f}})}{\partial z} + Z_{\mathrm{m}}RT\sum_{i=1}^{NC} m_i(z,t)$$
$$P_{\mathrm{f}} = \sum_{i=1}^{NC} P_{\mathrm{f}\_i} \tag{5}$$

For the coordinate system defined by Figure 5 with gases passing through specimens from the bottom to top, fracture gas velocity is governed by Darcy's law as follows:

$$\varepsilon_{\mathrm{f}}V = -\frac{K_{\mathrm{o}}}{\psi\mu_{\mathrm{m}}}\left[\frac{\partial P_{\mathrm{f}}}{\partial z} + g\rho_{\mathrm{m}}\right] = -\frac{K}{\mu_{\mathrm{m}}}\left[\frac{\partial P_{\mathrm{f}}}{\partial z} + g\rho_{\mathrm{m}}\right] \tag{6}$$

where μ_{m} and ρ_{m} are the viscosity and density for the gas mixture, respectively, K_{o} is the overall permeability based on the total cross section area of the specimen, K the permeability of cleats, V the gas velocity, g the gravitational acceleration, and $\psi > 1$ the correction parameter. The necessity for the incorporation of the correction parameter ψ is that, the Darcy flows occur not only in cleats but also in macro- and meso-pores. Without accounting for the contributions of other pore types to the permeability in addition to cleats, the velocity in cleats will be over estimated. The overall permeability in Eq. 6 is measured in our laboratory using the following approximation:

$$K_{\mathrm{o}} = \frac{Q_{\mathrm{m}}L\mu_{\mathrm{m}}}{A\Delta P} \tag{7}$$

where K_{o} is the overall permeability, Q_{m} the volumetric gas flow-rate at mean pore pressure, L and A the height and cross section area of coal specimens, respectively, and ΔP the total pressure drop.

The permeability can be estimated by using the following correlation for slit shaped fractures:

$$K = \frac{a^2}{12}\frac{\varepsilon}{\tau} = \frac{a^3}{12h}\frac{1}{\tau} = \frac{w^2}{3}\frac{\varepsilon}{\tau} \tag{8}$$

where a and w are the width and half width of slit fractures, respectively, h is the distance between fractures. With the application of the Archie's law, Eq. 8 becomes:

$$K = \frac{w^2}{3}\left(\frac{2w}{h}\right)^{\alpha} \tag{9}$$

Since the tortuosity τ of coal fractures is low, the parameter α is at the lower end of the value range as described previously. We use $\alpha = 1.4$ as a representative starting point.

The apertures of the fractures change dynamically because of adsorption induced swelling and the variations in external stresses. Consequently, the permeability also changes dynamically during CO_2 sequestration operations. This issue will be addressed in later sections.

A technique was proposed by Gilman and Beckie[10] to estimate single phase mass cross-flow rate with diffusion as the only mass transfer mechanism. It can be extended for the multicomponent systems with both of the diffusive and convective mass transfer fluxes as follows:

$$m_{\mathrm{i}} = \frac{D_{i,\mathrm{e}}}{Z_{\mathrm{m}}RT\lambda^2}(P_i - P_{\mathrm{f}\_i}) + \frac{K_{\mathrm{c}}}{\mu_{\mathrm{cm}}\lambda^2}(P_{\mathrm{c}} - P_{\mathrm{f}})C_i$$
$$= \frac{D_{i,\mathrm{e}}}{\lambda^2}(C_i - C_{\mathrm{f}\_i}) + \frac{K_{\mathrm{c}}}{\mu_{\mathrm{cm}}\lambda^2}(P_{\mathrm{c}} - P_{\mathrm{f}})C_i$$
$$i = 1, \ldots, NC \tag{10}$$

where $D_{i,\mathrm{e}}$ is the effective diffusivity for the computation of the diffusion mass transfer between the coal matrix and fractures, C_i is the gas phase concentration in the coal matrix, the subscript $i = 1, \ldots,$ NC is the index for identifying the species, K_{c} is the permeability of coal matrix in x-direction, P_{c}, and P_{f} are the total pressures in the coal matrix and fractures, respectively, μ_{cm} is the viscosity of gas mixture in the coal matrix, and λ is the half distance between fractures. This estimation method is easy to understand and simple to use. However, the original authors[10] could not explain the tremendous differences between the experimentally measured effective diffusivities and the Knudsen diffusivity. A rigorous mathematical analysis will be carried out in the sub-section titled Development of Effective Diffusivity for Model Simplification to address the issue of the observed discrepancy.

Adsorption Induced Dimensional Changes. The three dimensional strains are measured using strain gauges imbedded in coal specimens. There are two main inter-connected purposes for strain measurements: (1) to investigate coal compressibility in order to calculate the Young's modulus; and (2) to quantify adsorption/de-sorption induced coal swelling/shrinkage. A curve indicating variations of compressibility factor with average stress for a coal specimen is shown in Figure 6. The compressibility factor is defined as the inverse of the bulk modulus with the unit MPa^{-1}

The compressibility factor in the lower stress zone is used to estimate the Young's modulus of coal fractures, E_{f}, whereas that in the upper stress zone is used to estimate the Young's modulus of the coal matrix, E, using the following correlation:

$$\frac{1}{E_{\mathrm{t}}} = \frac{1}{E_{\mathrm{f}}} + \frac{1}{E} \tag{11}$$

where E_{t} is the total Young's modulus. An accurate estimation of E/E_{f} is essential for calculations of adsorption/desorption induced permeability variations, which will be described in the following sub-section.

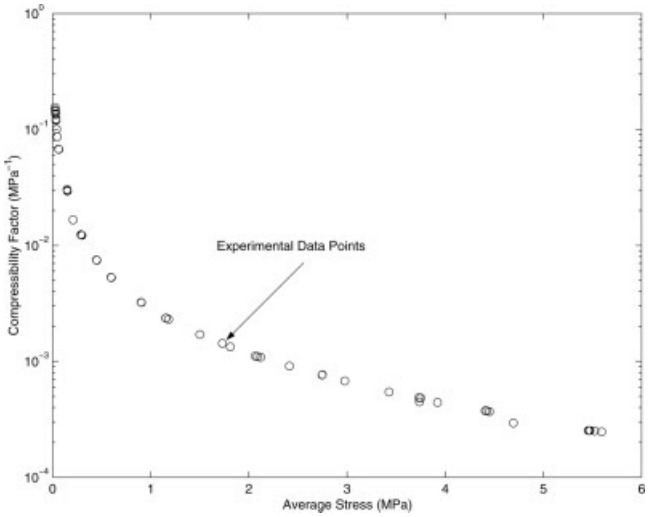

Figure 6. Variations of compressibility factor with average stress.

It has been realized for some time that coal specimens change sizes during adsorption/de-sorption processes, leading to significant permeability variations. Selected coal swelling data measured in our laboratory using the experimental rig shown in Figure 1 are listed in Table 1. The parameter γ in Table 1 is defined as the volumetric swelling coefficient for the computation of the volume change of coal specimens using the following equation[27]:

$$\Delta U = \gamma \Delta S \tag{12}$$

where ΔU and ΔS are changes of the specimen volume and adsorbed mass, respectively for constant external stresses. It can be seen that the dimensional changes take place in all of the three directions. Consequently, the condition of negligible lateral strain assumed by Gilman and Beckie[10] cannot be applied to our coal specimens.

Adsorption Induced Permeability Change. Gilman and Beckie[10] have developed a permeability model, which is presented in Appendix C. The model correlates the permeability variations with changes of the fracture pressure ΔP_f and the mass of adsorbed gases ΔS. The model provides certain physical insight and a starting point for further development. However, the computed values based on the model deviate from our measurement data significantly. Two main limitations associated with the Gilman and Beckie model can be identified as follows: (1) It is a static correlation without taking dynamic variations into account; and (2) The three main parameters, namely, γ, E, and E_f are treated as constants. We will show that these parameters are strong functions of adsorbed mass S, which should be considered in the modified model.

Our experimental rig is designed in such a way that the pressure in fractures can be controlled perfectly. Consequently, the condition of $\Delta P_f = 0$ can be assumed to simplify the model. Using differential calculus, the Gilman and Beckie model can be extended to the following more general format:

$$K(S) = K(S_0) \exp\left(\int_{S_0}^{S} -\frac{3\gamma(S)E}{(1-\nu)\tau_f E_f(S)} dS \right) \tag{13}$$

where τ_f is the tortuosity of cleats. Equation 13 provides more accurate prediction than the original model due to the following (1) Operations are not normally started from zero adsorption load; and (2) Both the Young's modulus for fractures E_f and the volumetric swelling coefficient are not constants, but functions of the adsorbed gas. As S is small, E_f could be very small leading to a large value of γ. On the other hand, E_f increases and γ decreases with the increase of S, leading to small variations of K as the system approaches adsorption saturation.

The aforementioned qualitative analysis can be justified using the measurement data shown in Table 1. The computed γ for the replacement of He by CH_4 under the mean pressure P_m = 2000 kPa is 2.5×10^{-4} (m^3/kg gas adsorbed). However, that for the replacement of CH_4 by CO_2 the value is only 1.3×10^{-4} (m^3/kg gas adsorbed), indicating the dependency of γ and E_f on the amount of the adsorbed gases. The γ values measured in our laboratory ($1.3–2.5 \times 10^{-4}$) are within the literature data range summarized by Van Krevelen.[27]

To compute permeability K using Eq. 13, it is necessary to determine the Young's moduli E and E_f in addition to γ. This can be done by measuring the compressibility factor of coal specimens. The range of compressibility factor of coal specimens is from 4.0×10^{-4}–1.0×10^{-1} MPa^{-1} with a typical curve shown in Figure 6. The median value is consistent with the literature value of 2.1×10^{-4} MPa^{-1} reported by Van Krevelen.[27] The lower and upper value sections are used for the estimation of E_f and E, respectively. From the measurements of compressibility for a number of coal specimens performed in our laboratory, the value range of E_f/E is 0.01–0.07 depending the extent of adsorption. It should be emphasized that for the dynamic processes, the values of γ and E_f/E must be changed dynamically according to the total amount of adsorbed gases. For example, if constant values of γ and E_f/E are used to estimate the permeability for CO_2 replacing CH_4 under 400 kPa, the computed per-

Table 1. Adsorption Induced Coal Specimen Swelling and Permeability Change

Property	CH_4 Replacing H_e		CO_2 Replacing CH_4	
Mean pressure P_m (kPa)	400	2000	400	2000
x-Direction strain ($\Delta L_x/L$)		0.0012		0.0019
y-Direction strain ($\Delta L_y/L$)		0.0010		0.0017
z-Direction strain ($\Delta L_z/L$)		0.0013		0.0020
Gas adsorbed (kg/m^3)	4.6	14.1	39.6	70.5
Permeability (mD)	3.1–3.2		1.9–2.1	0.8
Average γ (m^3/kg gas ads.)		2.5×10^{-4}		1.3×10^{-4}
Literature range of γ[27] (m^3/kg gas ads.)		$1.0–3.0 \times 10^{-4}$		

meability values differ from the real permeability (1.9–2.1 mD). This discrepancy can be effectively eliminated using Eq. 13 with adsorption dependent $\gamma(S)$ changing from 2.0×10^{-4} to 1.3×10^{-4} (m^3/kg gas adsorbed) and $E_f(S)/E(S)$ changing from 0.05 to 0.06.

An alternative technique for the determination of porosity/permeability variations for single component systems is based on the Palmer–Mansoori theory.[28] The limitation of the method is identified as: (1) It was originally developed for single component systems; and (2) Constant model parameters suggested in the original development lead to significant errors and inconsistencies. Further work is needed to extend the Palmer–Mansoori theory to multicomponent systems.

From the Gilman and Beckie model described by Eq. A4 with the assumption of negligible ΔP_f, the dynamic model of permeability is represented as:

$$\frac{dK}{dt} = -\frac{3\gamma(S)K(S)E}{(1-\nu)\tau_f E_f(S)}\frac{dS}{dt} \tag{14}$$

As for Eq. 13, K, E_f, and γ are all functions of S, and should also be estimated dynamically. The overall adsorption/de-sorption rate dS/dt is given by:

$$\frac{dS}{dt} = \sum_{i=1}^{NC}\left\{M_i\left(\frac{\int_0^L m_i(z,t)dz}{L} + N_i^{\text{in}} - N_i^{\text{out}}\right)\right\} \tag{15}$$

where M_i is the molecular weight for the i-th component, and m_i is the mole adsorption or de-sorption rate defined in Eq. 3 for the i-th component with either positive or negative sign, N_i^{in} and N_i^{out} are the total molar fluxes of the inlet ($z = 0$) and outlet ($z = \text{L}$) streams in z-direction for the species i consisting of five sub-fluxes, which will be further explained in the sub-section titled "Overall mass transfer model". Computations of the fluxes in z-directions will be described in the subsequent sections. The permeability variations with time, K(t), can be computed by solving the ordinary differential equation system given by Eqs. 14 and 15. A large number of measurement data have been obtained using the TTSCP in our laboratory. An example of the dynamic behavior of CO_2 replacing CH_4 for a typical case will be shown later.

Fluid Phase Diffusion in Porous Media (Fluxes 2 and 3). The fluid phase diffusions in macro and meso-pores consist of molecular diffusion and Knudsen diffusion. The molar fluxes within the macro and meso-pores in the Dusty-Gas model format with the porosities defined in Eq. 1 are represented as:

$$\begin{aligned}\mathbf{N}_{\text{dma}} &= -\frac{\varepsilon_{\text{ma}}}{\tau_{\text{ma}}}\left(\mathbf{B}_{\text{ma}}^{-1}\frac{\partial \mathbf{C}}{\partial z}\right)\\ \mathbf{N}_{\text{dme}} &= -\frac{(1-\varepsilon_{\text{ma}})\varepsilon_{\text{me}}}{\tau_{\text{me}}}\left(\mathbf{B}_{\text{ma}}^{-1}\frac{\partial \mathbf{C}}{\partial z}\right)\end{aligned} \tag{16}$$

The general form for Stefan-Maxwell matrix $\boldsymbol{B}$ is given by:

$$\begin{aligned}B(i,i) &= \frac{1}{D_{\text{ki,e}}^{E-F}} + \sum_{\substack{n=1\\ n\neq i}}^{nc}\frac{y_n}{D_{in,\text{e}}^{E-F}}; i = 1,\ldots,NC,\\ B(i,j) &= -\frac{y_i}{D_{ij,\text{e}}^{E-F}}, i,j = 1,\ldots,NC; i \neq j.\end{aligned} \tag{17}$$

The EMT–SFA is employed to address diffusion in meso-pore networks. To simplify the computations, we assume a uniform pore length. This is because the real pore length distribution cannot be measured, and a nonuniform pore length distribution can be accounted for by adjusting the ε/τ value in the parameter identification procedures. The proposed methods can be extended to include pore length distribution if known. For a network of uniform length pores, the EMT-FSA Knudsen diffusivity for slit shape pores is given by:

$$\begin{aligned}D_{Ki,\text{e}}^{E-S} &= \frac{1}{\tau}\varepsilon\, Q_i\frac{\langle w^3\rangle_{\text{e}}}{\langle w^2\rangle}\\ Q_i &= \frac{1}{2}\sqrt{\frac{8RT}{\pi M_i \times 10^{-3}}}\end{aligned} \tag{18}$$

The EMT–FSA effective binary diffusivity in slit pores takes the following form:

$$D_{ij,\text{e}}^{E-S} = \frac{1}{\tau}\varepsilon\, D_{ij}\frac{\langle w^2\rangle_{\text{e}}}{\langle w^2\rangle} \tag{19}$$

In Eqs. 18 and 19, the effective average is defined as:

$$\langle q^a\rangle_{\text{e}} = \int_{q_{\min}}^{q_{\max}} q^a f(q)dq \tag{20}$$

where $f(q)$ is a distribution function such as the lognormal and Γ-distribution functions given by Eqs. A2 and A3 in Appendix B, respectively, $q_{\min}$, and $q_{\max}$ are the minimum and maximum values of q, respectively. The arithmetic average is represented as follows:

$$\langle q^a\rangle = \frac{1}{q_{\max}}\int_{q_{\min}}^{q_{\max}} q^a\, dq \tag{21}$$

Viscous Flows in Porous Media (Fluxes 4 and 5). The molar fluxes of viscous flows within the macro and meso-pores are given by:

$$\begin{aligned}\mathbf{N}_{\text{vma}} &= -\frac{\varepsilon_{\text{ma}}}{\tau_{\text{ma}}}\frac{B_{\text{ma0}}Z_{\text{m}}RT}{\mu_{\text{m}}}\frac{\partial C}{\partial z}\mathbf{B}_{\text{ma}}^{-1}\Lambda_{\text{ma}}\mathbf{C}\\ N_{\text{vme}} &= -\frac{(1-\varepsilon_{\text{ma}})\varepsilon_{\text{me}}}{\tau_{\text{me}}}\frac{B_{\text{me0}}Z_{\text{m}}RT}{\mu_{\text{m}}}\frac{\partial C}{\partial z}\mathbf{B}_{\text{me}}^{-1}\Lambda_{\text{me}}\mathbf{C}\end{aligned} \tag{22}$$

The generalized form of the diagonal matrix Λ is given by:

$$\begin{aligned}\Lambda(i,i) &= \frac{1}{D_{ki,\text{e}}^{E-F}}, i,j = 1,\ldots,nc,\\ \Lambda(i,j) &= 0; i \neq j.\end{aligned} \tag{23}$$

Equation 23 is applicable to both macro and meso-pores with respective Knudsen diffusivities. The permeability parameters B_{ma0} and B_{me0} in Eq. 22 are computed using:

$$\begin{aligned}B_{\text{ma0}} &= \frac{1}{3}\frac{\langle w_{\text{ma}}^4\rangle_{\text{e}}}{\langle w_{\text{ma}}^2\rangle}\\ B_{\text{me0}} &= \frac{1}{3}\frac{\langle w_{\text{me}}^4\rangle_{\text{e}}}{\langle w_{\text{me}}^2\rangle}\end{aligned} \tag{24}$$

Surface Diffusion Model (Flux 6). We separate cleats from other pores and combine the micro-pores with the solid phase. Consequently, the total porosity is only contributed by macro- and meso-pores defined by Eq. 1. We also imbed the tortuosity of micro-pores into the surface diffusivity to make it consistent with the majority of publications in the adsorption literature. The local surface flux of each species can be written respectively in terms of the hypothetical and the adsorption concentration as[16]:

$$J_{\mu,i}(w) = -D_{\mu,i}(w)\frac{C_{\mu,i}(w)}{C_{\mathrm{hy},i}}\sum_{j=1}^{NC}\frac{\partial C_{\mathrm{hy},i}}{\partial C_{\mu,j}(w)}\nabla C_{\mu,j}(w) \tag{25}$$

where $C_{\mathrm{hy},i}$ and $C_{\mu,i}$ are the hypothetic bulk concentration and adsorbed phase concentration for component i, respectively. The representation of $C_{\mathrm{hy},i}$ was developed by Wang and Do[16] based on the extended Langmuir isotherm. However, since the coal surfaces are not uniform, it may be better to use the extended hybrid Langmuir–Freundlich equation explained by Yang[6] in adsorption studies for coals. Consequently, the hypothetic bulk concentration becomes:

$$C_{\mathrm{hy},i} = \frac{1}{b_i(w)}\left[\frac{C_{\mu,i}(w)}{C_{\mu\mathrm{s},i} - \sum_{j=1}^{NC} C_{\mu,j}(w)}\right]^{1/\eta_i} \tag{26}$$

The derivation of Eq. 26 is shown in Appendix D. In Eq. 26, η_i, $i = 1, \ldots, \mathrm{NC}$, are additional parameters in the extended hybrid Langmuir–Freundlich equation, which will be described later, and the pore size-dependent parameter b_i is defined as:

$$b_i(w) = \frac{k_{\mathrm{ads}}(i)}{k_{\mathrm{des}}(i,w)}\exp\left[\frac{E(i,w)}{RT}\right] = \frac{\beta}{\sqrt{M_i T}}\exp\left[\frac{E(i,w)}{RT}\right] \tag{27}$$

In Eq. 27, k_{ads} and k_{des} are adsorption and de-sorption rate constants, respectively, E is the adsorption energy, and parameter β is assumed to be solid specific and independent with respect to adsorbate. The surface diffusion model is then formulated as:

$$\frac{\partial C_{\mu,i}(w)}{\partial t} = \frac{1}{z^s}\frac{\partial}{\partial z}\left(z^s D_{\mu,i}(w)\frac{C_{\mu,i}(w)}{C_{\mathrm{hy},i}}\sum_{j=1}^{NC}\frac{\partial C_{\mathrm{hy},i}}{\partial C_{\mu,j}(w)}\nabla C_{\mu,j}(w)\right) \tag{28}$$

where s is defined as the geometric factor with values of s = 0, 1, 2 for slab, cylinder and sphere, respectively; and the adsorbed phase diffusivity $D_{\mu i}$(w) is given by:

$$D_{\mu,i}(w) = D^0_{\mu i,\infty}\exp\left[-\frac{a_i E_i(w)}{RT}\right] \tag{29}$$

In Eq. 29, a is the ratio of activation energy for surface diffusion to adsorption energy,[16] $D^0_{\mu,\infty}$ is the surface diffusivity at zero loading and infinite temperature. Both a and $D^0_{\mu,\infty}$ are normally treated as fitting parameters. The equilibrium adsorption is computed by using the extended hybrid Langmuir-Freundlich equation[6] expressed as:

$$C_{\mu,i}(w) = C_{\mu\mathrm{s},i}\frac{b_i(w)C_i^{\eta_i}}{1 + \sum_{j=1}^{NC} b_j(w)C_j^{\eta_j}} \tag{30}$$

where $C_{\mu\mathrm{s},i}$ is the adsorption capacity for component i with the following temperature dependent form:

$$C_{\mu\mathrm{s},i} = C_{\mu\mathrm{s}0,i}\exp[\delta_i(T - T_0)] \tag{31}$$

in which $C_{\mu\mathrm{s}0,i}$ and δ_i represent adsorbed capacity at reference temperature (273 K) and temperature dependent coefficient of adsorption capacity, respectively, for species i. Equation 30 can be rewritten in the matrix model format as:

$$\mathbf{J}_\mu(w) = -(1-\varepsilon_\mathrm{t})\mathbf{D}_\mu(w)\frac{\partial \mathbf{C_{hy}}}{\partial \mathbf{C}_\mu^T}(w)\nabla \mathbf{C}_\mu(w) \tag{32}$$

where the total porosity ε_t is defined in Eq. 1 without counting the micro-porosity, and $\mathbf{D}_\mu$(w) is a diagonal matrix defined as:

$$\mathbf{D}_\mu(w) = \begin{bmatrix} D_{\mu,1}(w)\frac{C_{\mu,1}(w)}{C_{\mathrm{hy},1}} & 0 & 0 \\ 0 & \ddots & 0 \\ 0 & 0 & D_{\mu,\mathrm{NC}}(w)\frac{C_{\mu,\mathrm{NC}}(w)}{C_{\mathrm{hy,NC}}} \end{bmatrix} \tag{33}$$

and the vector differentiation is given by:

$$\frac{\partial \mathbf{C_{hy}}}{\partial \mathbf{C}_\mu^T}(w) = \begin{bmatrix} \frac{\partial C_{\mathrm{hy},1}}{\partial C_{\mu,1}(w)} & \cdots & \frac{\partial C_{\mathrm{hy},1}}{\partial C_{\mu,\mathrm{NC}}(w)} \\ \vdots & \ddots & \vdots \\ \frac{\partial C_{\mathrm{hy,NC}}}{\partial C_{\mu,1}(w)} & \cdots & \frac{\partial C_{\mathrm{hy,NC}}}{\partial C_{\mu,\mathrm{NC}}(w)} \end{bmatrix} \tag{34}$$

Overall Mass Transfer Model. The mass transfer model within coal blocks consisting of five mass fluxes is developed as:

$$\varepsilon_\mathrm{t}\frac{\partial \mathbf{C}}{\partial \mathrm{t}} + (1-\varepsilon_\mathrm{t})\frac{\partial \langle \mathbf{C}_\mu\rangle_\mathrm{e}}{\partial t} = -\frac{1}{z^s}\frac{\partial}{\partial z}\left\{z^s\left[\mathbf{N}_\mathrm{dma} + \mathbf{N}_\mathrm{vma} + \mathbf{N}_\mathrm{dme} + \mathbf{N}_\mathrm{vme} + \langle \mathbf{J}_\mu\rangle_\mathrm{e}\right]\right\} - \mathbf{m} \tag{35}$$

where vector $\mathbf{m}$ is defined in Eq. 3. The overall mass transfer model consists of the submodel for fluid flow (Flux 1) in cleats described by Eq. 3 and the mass transfer sub-model within coal blocks represented by Eq. 35. The five mass fluxes in coal blocks (Fluxes 2–6) are defined in Eqs. 16, 22, and 32 respectively. The major advantage to combine the mass transfer in micro-, meso- and macro-pores together is the elimination of the computation of the mass transfer between the micro-pores and other two pore types. The time derivative term of $\mathbf{C}_\mu$ in Eq. 35 is given by:

$$\frac{\partial \langle \mathbf{C}_\mu\rangle_\mathrm{e}}{\partial t} = \left\langle \frac{\partial \mathbf{C}_\mu}{\partial \mathbf{C}^T}\right\rangle_\mathrm{e}\frac{\partial \mathbf{C}}{\partial t} \tag{36}$$

where

$$\left\langle \frac{\partial \mathbf{C}_\mu}{\partial \mathbf{C}^T} \right\rangle_e = \left\langle \begin{bmatrix} \frac{\partial C_{\mu 1}(w)}{\partial C_1} & \cdots & \frac{\partial C_{\mu 1}(w)}{\partial C_{nc}} \\ \vdots & \ddots & \vdots \\ \frac{\partial C_{\mu nc}(w)}{\partial C_1} & \cdots & \frac{\partial C_{\mu nc}(w)}{\partial C_{nc}} \end{bmatrix} \right\rangle_e \tag{37}$$

Consequently, the overall mass transfer model described by Eq. 35 becomes:

$$\left\{ \varepsilon_t \mathbf{I} + (1-\varepsilon_t) \left\langle \frac{\partial \mathbf{C}_\mu}{\partial \mathbf{C}^T} \right\rangle_e \right\} \frac{\partial \mathbf{C}}{\partial t} = -\frac{1}{z^s} \frac{\partial}{\partial z} \{ z^s [\mathbf{N}_{dma} + \mathbf{N}_{vma} + \mathbf{N}_{dme} + \mathbf{N}_{vme} + \langle \mathbf{J}_\mu \rangle_e] \} - \mathbf{m} \tag{38}$$

where $\mathbf{I}$ represents an identity matrix. The effective average is defined by Eq. 20.

N_i^{in} and N_i^{out} in Eq. 15 are the summations of the five fluxes for component i at the two boundaries ($z = 0$ and $z =$ L), which can be readily computed using the boundary conditions of Eq. 38 without the necessity to add additional terms in the model.

Development of Effective Diffusivity for Model Simplification. There are three types of diffusivities in the system, namely diffusivities in micro- and meso-pores, and surface diffusivity. A very common practice is the development of a unique effective diffusivity to replace all three diffusivities.[10] It should be pointed out that the effective diffusivity developed for the combination of different diffusivities is different from the effective EMT-FSA diffusivity defined by Eqs. 18 and 19. Normally the effective diffusivities are estimated using the experimental data. In general, they are many orders of magnitude less than Knudsen and molecular diffusivities. They are sometimes denoted as "pseudo diffusivities."[6] There are no convincing physical explanations for the tremendous discrepancies between the effective and mechanistically based diffusivities. This inconsistency is analyzed rigorously as follows.

Without losing generality, we demonstrate the derivation of the effective diffusivity for a single component system consisting of two pore types, namely micro- and macro-pores for notational simplicity. The overall mass balance is given by:

$$\varepsilon_t \frac{\partial C}{\partial t} + (1-\varepsilon_t) \frac{\partial C_\mu}{\partial t} = \frac{\varepsilon_t}{\tau} D \frac{\partial^2 C}{\partial z^2} + (1-\varepsilon_t) D_\mu \frac{\partial^2 C_\mu}{\partial z^2} + \cdots \tag{39}$$

Partial derivatives of C_μ are derived as:

$$\frac{\partial C_\mu}{\partial t} = \frac{\partial C_\mu}{\partial C} \frac{\partial C}{\partial t}$$
$$\frac{\partial^2 C_\mu}{\partial z^2} = \frac{\partial C_\mu}{\partial C} \frac{\partial^2 C}{\partial z^2} + \frac{\partial C}{\partial z} \frac{\partial}{\partial z} \left(\frac{\partial C_\mu}{\partial C} \right) \tag{40}$$

Substitute Eq. 40 into Eq. 39, after algebraic operations, we obtain:

$$\frac{\partial C}{\partial t} = \frac{\frac{\varepsilon_t}{\tau} D + (1-\varepsilon_t) \frac{\partial C_\mu}{\partial C} D_\mu}{\varepsilon_t + (1-\varepsilon_t) \frac{\partial C_\mu}{\partial C}} \frac{\partial^2 C}{\partial z^2} + \frac{(1-\varepsilon_t) D_\mu \frac{\partial}{\partial z} \left(\frac{\partial C_\mu}{\partial C} \right)}{\varepsilon_t + (1-\varepsilon_t) \frac{\partial C_\mu}{\partial C}} \frac{\partial C}{\partial z} + \cdots \tag{41}$$

Consequently, the effective diffusivity should be defined as:

$$D_e = \frac{\frac{\varepsilon_t}{\tau} D + (1-\varepsilon_t) \frac{\partial C_\mu}{\partial C} D_\mu}{\varepsilon_t + (1-\varepsilon_t) \frac{\partial C_\mu}{\partial C}} \tag{42}$$

Since the total porosity ε_t is defined by Eq. 1 without counting the micro-porosity, it is very small for coal specimens. We may use $\varepsilon_t = 0.03$ to perform illustrative computations. The effective diffusivity could be in the range of 10^{-10} to 10^{-13} m^2/s for the proper combinations of the values of ε_t, τ, and $\partial C_\mu / \partial C$. The concentration (or partial pressure) dependency of the effective diffusivity is partly accounted for through the derivative term $\partial C_\mu / \partial C$. However, the possible change of the connectivity because of pressure variations suggested by Gilman and Beckie[10] has not been justified experimentally. The experimentally determined effective diffusivities lead to reasonable predictions of diffusion processes in coal with certain sacrifice in physical insights.

Through the development of the effective diffusivity, the diffusion processes in three pore types are reduced to a single diffusion processes, leading to a significant model simplification. The overall effective diffusivity can be estimated using Eq. 42 without purely relying on experimental measurements. We use effective diffusivity described by Eq. 42 only in the computation of mass transfer between coal matrix and cleats. To keep the mathematical rigor and numerical accuracy, individual diffusivities are used in mass transfer computations within the coal matrix.

The effective diffusivity represented by Eq. 42 should be used with caution since the embedded simplifications may introduce errors that are not negligible. The method should be compared with 2D and 3D models that include rigorous computations of the individual flux in various directions to verify its applicability for particular systems.

Mechanisms of coal swelling in adsorption processes

It has long been recognized that adsorption in porous materials is accompanied by adsorption deformation.[8] We show in the previous section that this deformation affects coal permeability significantly, a result suggesting increased research in the relevant areas for CBM and ECBM processes. In spite of the advances achieved in the areas of sorption induced deformation, the mechanisms leading to this practically important phenomenon are only known very approximately. Based on previous research, including comprehensive mechanistic studies carried out at The University of Queensland, we propose three major mechanisms in this section.

Adsorption Induced Carbon Bond Extension: Basal Plane Enlargement. Through molecular orbital theory calculations using the software package Gaussian 98, Zhu et al.,[29] have observed carbon-carbon (C—C) bond extensions during hydrogen adsorption processes. In that work, three types of adsorption sites on single layer graphite are investigated: (1) the "on-top site" directly above a carbon atom (called t site); (2) the "bridging site" above a C—C bond (called b site); and (3) the "middle hollow site" above a hexagon (called m site). These different sites are graphically shown in the original article.[29] The following two models were proposed in the

previous study: model 1-A has an odd electron number with an open-shell electronic state, and model 2-B has an even electron number with a closed-shell electronic state. A very important and consistent observation is that the adjacent C—C bond of the anchoring carbon of model 1-A has extended from ca. 1.42 Å before H adsorption to ca. 1.51 Å after H adsorption. This implies about 7% C—C bond extension in the H adsorption process. Of course, the single C—C bond extension does not completely contribute to the overall coal size enlargement. Because of the complexity of graphite and pore arrangements in coals, only a minor part of the bond extension is shown in the overall coal size enlargement because of space confinement and energy dissipation. However, there is no doubt that the C—C bond extension during adsorption is an important mechanism for the adsorption induced coal dimensional change. It should be noted that the C—C bond extension is mainly along the basal plane. The edge-site plane deformation will be explained in the next section.

Adsorption Induced Solvation Pressure Variation: Edge-Site Plane Deformation. Ustinov and Do[8] believe that the solvation pressure due to adsorption of fluids in porous materials is the cause of elastic deformation of an adsorbent. Such a deformation contributes to the Helmholtz free energy of the whole adsorbent-adsorbate system due to accumulation of compression or tension energy by the solid. It means that in the general case the solid has to be considered as not solely a source of the external potential field for the fluid confined in the pore volume, but also as a thermodynamically non-inert component of the solid-fluid system. They presented analysis of nitrogen adsorption isotherms and heat of adsorption in slit graphitic pores accounting for the adsorption deformation by means of non-local density function theory (NLDFT). The solvation pressure p_s is defined as follows:

$$p_s = \Delta\Pi - p_b = \Pi_{ss} + \Pi_{sf} - \Pi_0 - p_b \tag{43}$$

where p_b is the bulk pressure, Π_0 the initial pressure at zero loading acting between pore walls separated by an initial distance H_0, Π_{ss} the pressure acting between pore walls at non-zero loadings with pore size variations, and Π_{sf} the pressure acting on pore walls by fluids. Although the analysis was carried out for idealized systems at low temperature (77 K), the single pore deformation data reported by Ustinov and Do[8] are very useful for the study of the mechanisms of adsorption deformation. We assume that the Young's modulus of coal matrix is 3 GPa. There is about 13% pore size enlargement for a pore with initial width of 6.1 Å. The deformation is more pronounced for larger pores with the same Young's modulus. For example, 21% pore size enlargement for a pore with initial width as 8.4 Å is estimated based on the computations carried out by Ustinov and Do.[8]

Through a comparative study between basal plane and edge-site plane deformations, it can be shown that although the latter is more significant than the former, the extension along the basal plane is far from negligible.

Adsorption Induced Carbon-Metal Bond Extension. There are a significant number of metal atoms adsorbed on the inner surfaces of coals. It has been demonstrated experimentally[30] that the Pt-C bond is reduced from 2.62 Å to 2.02 Å after the removal of the atomically adsorbed hydrogen in the interface between the metal particles and the carbon support. The change is as big as 30%. It can be surmised that this also happens to other metal-carbon bonds resulting in similarly significant dimensional changes. Further studies are necessary in this area and we are pursuing detailed studies on metal-carbon bonds using the ab initio method to obtain accurate predictions of metal-carbon bond lengths.[31]

The three mechanisms coexist, playing different roles. We speculate that the adsorption induced carbon bond extension quantified by the authors[29] could be the dominant mechanism for coal permeability variations. Edge-site plane deformation due to the solvation pressure change[8] and the carbon-metal bond extension[30,31] in adsorption processes may mainly affect mass transfer in micro-pores with relatively small effects on cleat permeability. We reason as follows: (1) The length of the basal plane is larger than that of the edge-site plane, leading to the broadened stress transmission and strain propagation; (2) Because of the softness of the edge-site plane and carbon-metal bonds, deformation may cause porosity relocations within the coal matrix before reaching the cleat zones. In contrast to the edge-site plane, the stiffness and high density of the basal plane provide relatively smaller opportunity for the deformation to be tolerated within the coal matrix.

It should be pointed out that microscopic level studies on adsorption deformations are carried out to explore the deformation mechanisms. The quantitative values above cannot be directly applied to macroscopic level coal swelling/shrinkage in sorption processes because of the complexity of coal structures. However, the mechanistic understanding of adsorption induced coal size changes will certainly help us to develop physically based models in the near future.

Physical properties and numerical scheme

Computation of Physical Properties. In this work, the physical properties are computed dynamically as part of the simulation objectives rather than pre-specified parameters or averaged values. The main physical properties of gases are estimated using methods and working equations recommended and detailed in Reid et al.,[32] which are briefly explained in Appendix E. There is no rigorous method for the computation of surface diffusivities without carrying out molecular simulations for idealized systems.[33] However, it is very interesting to note that the surface diffusivity in a cylindrical pore without accounting for the effects of porosity and tortuosity is in the same order of magnitude as the self diffusivity (10^{-9} to 10^{-8} m^2/sec). Consequently, self diffusivities can be used as the starting point for the estimation of $D^0_{\mu\infty}$. A simple method for the computation of the self diffusivity was developed by Mathur and Thodos,[34] which is also presented in Appendix E.

Numerical Scheme. Because of the complexity of the problem, the numerical scheme covers a broad range of computational techniques. These mainly include the reduction of partial differential equations (PDE) with moving front into ordinary differential-algebraic equations (DAE); solution of large-scale, stiff DAE systems; operations of multi-dimensional arrays with up to 4 argument (k, l, i, j) where k, l, i,

and j indicate the spatial location, pore size, species i and species j, respectively; symbolic differentiations; computations of physicochemical properties; and parameter identification using dynamic optimisation algorithms. A detailed explanation on each of the method exceeds the main scope of the current contribution. Only the most important ones are briefly described in this section.

The matrix form partial differential equations (PDE) in the mathematical model are discretised by using the method of orthogonal collocation on finite elements (OCFE) to form a set of ordinary differential equations with nonlinear algebraic constraints. This numerical scheme has been well explained by Finlayson,[35] as well as Villadsen and Michelsen.[36] The method can be briefly described as division of the spatial domain into a number of finite elements followed by a further discretisation of each element by using the orthogonal collocation method. We use a simplified matrix model to demonstrate the method. Assume that the matrix model is described by:

$$\frac{\partial \mathbf{x}}{\partial t} = \frac{1}{\varsigma^s}\frac{\partial}{\partial \varsigma}\left(\varsigma^s \mathbf{B}^{-1}\frac{\partial \mathbf{x}}{\partial \varsigma}\right) + \frac{1}{\varsigma^s}\frac{\partial}{\partial \varsigma}(\varsigma^s V\mathbf{x}) + \mathbf{R} \tag{44}$$

where $\mathbf{x}$ and $\mathbf{R}$ are column vectors with NC elements in each vector representing component concentration and mass generation rate, respectively, $\mathbf{B}$ is a square Stefan-Maxwell matrix with NC rows and columns, and ζ is the dimensionless spatial variable defined in [0,1]. In each finite element, the spatial interval must be converted into [0,1] in order to apply the orthogonal collocation method. Using the notation $\mathbf{IB}$ to replace $\mathbf{B}^{-1}$, the ordinary differential equation (ODE) for the i-th component in the k-th collocation point is represented by:

$$\frac{dx_i(t,\varsigma_k)}{dt} = \frac{1}{\varsigma_\varsigma^s}\mathbf{A}_k\left\{\begin{bmatrix} \varsigma_1^s \mathbf{IB}_1(i,1:NC)\frac{\partial \mathbf{x}}{\partial \varsigma}\Big|_k \\ \vdots \\ \varsigma_n^s \mathbf{IB}_n(i,1:NC)\frac{\partial \mathbf{x}}{\partial \varsigma}\Big|_k \end{bmatrix} + V\begin{bmatrix} \varsigma_1^s x_i(\varsigma_1) \\ \vdots \\ \varsigma_n^s x_i(\varsigma_n) \end{bmatrix}\right\} + R(t,\varsigma_k) \tag{45}$$

where n is the number of collocation points, $\mathbf{A}_k$, $k = 1,2, \ldots, n$ are the k-th row in the collocation matrix $\mathbf{A}$, $\mathbf{IB}_k$ represent the matrix $\mathbf{IB}$ at the k-th collocation point, the notation "1:NC" represents "from the column 1 to the column NC", and the spatial derivative at the k-th collocation point can be computed by using:

$$\frac{\partial \mathbf{x}}{\partial \varsigma}\Big|_k = \begin{bmatrix} \mathbf{A}_k\mathbf{x}_1 \\ \vdots \\ \mathbf{A}_k\mathbf{x}_{NC} \end{bmatrix}$$

$$\mathbf{x}_j = \begin{bmatrix} x_j(\varsigma_1) \\ \vdots \\ x_j(\varsigma_n) \end{bmatrix}; \quad \begin{matrix} k = 1,2,\ldots,n \\ j = 1,2,\ldots,NC \end{matrix} \tag{46}$$

The spatial derivatives in the boundary conditions can also be formulated using the collocation matrix $\mathbf{A}$. Although the actual mass balance equations, consisting of molecular and Knudsen diffusions as well as viscous flow within macro- and meso-pores, and surface diffusion in micro-pores, are much more involved than this simple example, the mathematical principles used in the numerical computations are the same.

In numerical computations, $\mathbf{IB}$ is treated as a three-dimensional array with $k = 1,2, \ldots$ n, to indicate spatial location, and $i, j = 1,2, \ldots$, NC to identify components. It should be pointed out that computations of mass transfer in micro-pores involve the handling of 4-dimentional arrays with the argument (k, l, i, j) defined previously. For example, if we identify CH_4, CO_2, and N_2 as the first, second and third component (i, $j = 1, 2, 3$), respectively, then $C_\mu(2, 3, 1, 1{:}3)$ provides the following information: location specification, which is at the 2nd collocation point; micro-pore size specification, which is in the 3rd size class; component specification, which is for the species CH_4; and interaction specification, which interacts with 3 components (including itself). The same strategy is used for J_μ computations.

The resulting differential-algebraic (DAE) system for the actual process is of the general form as follows:

$$\mathbf{M}(\mathbf{x})\frac{d\mathbf{x}}{dt} = \mathbf{F}(\mathbf{x}) \tag{47}$$

where $\mathbf{M(x)}$ is a singular, sparse and state-dependent mass matrix; and $\mathbf{F}$ the vector function. The large-scale DAE system is solved by using ode15s.m in MATLAB.

It should be pointed out that there is a discontinuity at the inlet boundary due to the step change of the CO_2 concentration. Numerical difficulties are encountered by using the fixed boundary OCFE methods for large step changes. There are two ways to solve the problem, namely (1) increase the number of finite elements; and (2) using special numerical methods for solving problems with moving fronts, described by Finlayson.[37] Compared with method (1), the moving front approach leads to a smaller model order. The method requires the determination of the location of the mass front in the coal matrix. This can be done by using Darcy's law in the coal matrix represented by Eq. 6 with appropriate values of the permeability computed using Eqs. 8 or 9. As soon as the moving boundary is located, the coal specimen can be divided into two zones before and after the moving front. For small step changes, such as to step up the CO_2 mole fraction from 0.8 to 1.0, two fixed-size finite elements can be used for the solution of the problem without leading to severe Gibbs oscillations.

Results and Discussion

Dynamic variations of permeability

The dynamic permeability variations during a CO_2 replacing CH_4 process at the mean pressure as 400 kPa are depicted in Figure 7. The experimentally measured dynamic behavior is compared with simulation results based on two different models, namely the mechanistic model and the black-box ARX (Auto-Regressive Exogeneous) model. The mechanistic model is defined as the model described by Eqs. 14 and 15, and the single input, single output black-box ARX model is given by[38]:

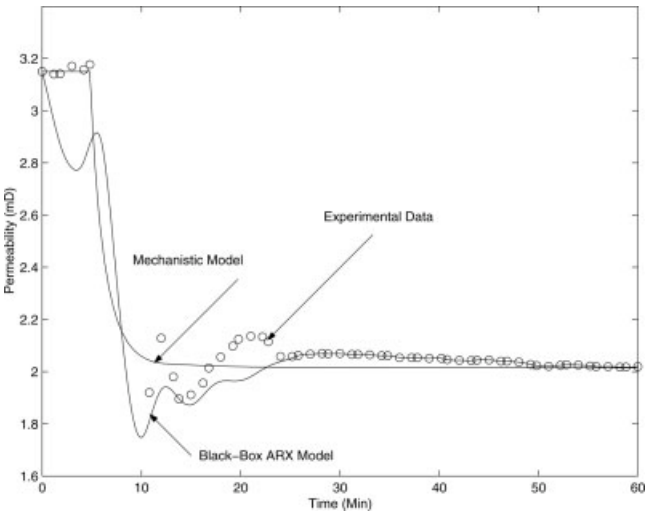

Figure 7. Dynamics of permeability variations.

$$y(t) + a_1 y(t-1) + \cdots + a_{n_a} y(t-n_a) = b_1 u(t-1) + \cdots + b_{n_b} u(t-n_b) + e(t) \quad (48)$$

where u and y are input and output variables, respectively, e is the disturbance, a and b are time varying coefficients identified online, n_a and n_b are defined as prediction and control horizons.

From Figure 7, it can be seen that both mechanistic and black-box models predict the trend very well. However, the measurement data show significant oscillations before reaching the final steady state, which are not predicted by the mechanistic model. The oscillations could be caused by the following three mechanisms: (1) the concept of the relative permeability because of different properties of CH_4 and CO_2; (2) damped mechanical vibrations around the equilibrium position; and (3) locally higher adsorption densities near the cleat areas. Further work is needed to justify the oscillation mechanisms and to incorporate these mechanisms into the mechanistic model.

Since the black-box ARX model described by Eq. 48 is a linear modeling strategy, and the measured dynamic behavior shows certain nonlinearity, two different ARX model structures are used in the time intervals 0–25 and 25–60 min, respectively. Although multiple black-box models are able to predict the oscillation behavior, the parameters in the models do not possess clear physical significance. The reasonable prediction results are obtained from proper data training algorithms. Consequently, if the main purpose of model simulations is to gain physical insights regarding the process, mechanistic models are obviously preferred.

The dramatic permeability drop shown in Figure 7 is caused by large E/E_f ratio incorporated in Eqs. 13 and 14. At early adsorption stage, the Young's modulus of fractures, E_f, is about two orders of magnitude smaller than that of the coal matrix. Consequently, very fast dynamics can be observed.

Fluid flow in cleats

Simulations on fluid flow in cleats are performed using the mass balance model described by Eqs. 3–6, and 10 together with the model accounting for the permeability variations during adsorption/de-sorption processes represented by Eqs. 14 and 15. There are two ways to address the mass transfer between coal matrix and the in-cleat fluid stream, namely pure distributed parameter model and hybrid distributed-lumped parameter model. In the hybrid distributed-lumped parameter model, the fluid flow in cleats is represented by the distributed parameter model and the adsorbed gas variations in the matrix are described by the lumped parameter model as suggested by Gilman and Beckie.[10] Compared with the pure distributed parameter model, the hybrid modeling technique reduces computational load considerably with the sacrifice of physical insights. The effective diffusivities should be adjusted based on the measurement data. We display selected simulation results using the pure distributed parameter model to show the main characteristics of fluid flow in cleats. The downstream mole fractions for both CH_4 and CO_2 are shown in Figure 8 for experiment in which CO_2 is displacing CH_4. It can be seen that the simulated results agree with the measured data reasonably well. Although the hybrid distributed-lumped parameter model is also able to predict the dynamic behavior with acceptable error tolerance, two main advantages for the use of the pure distributed parameter model can be identified as: (1) the effective diffusivities can be computed using Eq. 42 without the incorporation of adjustable parameters; and (2) the dynamic variations of CH_4 and CO_2 in the coal matrix can be investigated in detail, which could be important for the development of improved operational conditions.

Two 3D diagrams for CH_4 and CO_2 variations in cleats are depicted in Figures 9a, b, respectively. These figures indicate that the variations of gas concentrations with time are much more significant that with spatial locations. This implies that the fluid flow in cleats can be classified as a process with fast dynamics. On the other hand, the fluid flow and molecular diffusion in macro- and meso-pores can be classified as processes with medium dynamics, and the surface diffusion within micro-pores is very slow. This will be demonstrated and analyzed in nest section.

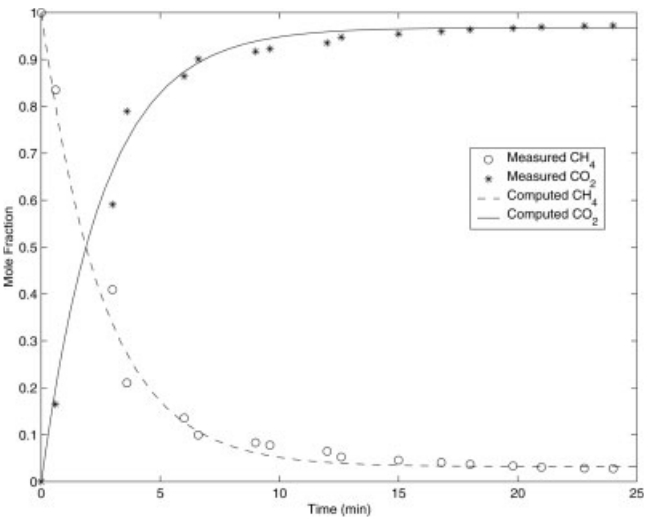

Figure 8. Variations of down stream mole fractions.

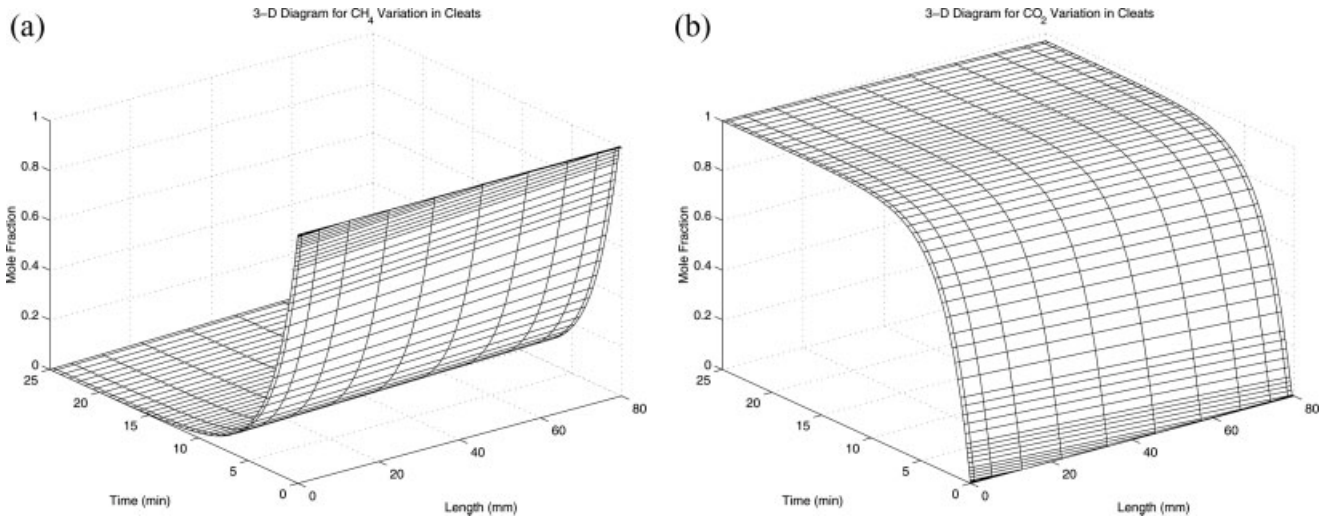

Figure 9. (a) Three-dimensional diagram for CH_4 dynamics in cleats; (b) three-dimensional diagram for CO_2 dynamics in cleats.

Mass transfer in coal matrix

Comprehensive numerical simulations have been carried for the investigation of mass transfer in coal matrix based on the model described by Eqs. 16–38. We only report the results for a typical coal specimen under the conditions of mean pressure, 400 kPa and temperature, 25°C. The nominal values in the adsorption-diffusion model are listed in Table 2.

In contrast to fast dynamics depicted in Figures 8 and 9 for fluid flow in cleats, mass transfer processes in the coal matrix are slow. In particular, the lower the residual CH_4 remaining in the coal specimen, the slower the mass transfer rates. In order to take a close observation of the concentration variations within the coal matrix at later stages, we carry out simulations with the initial conditions set as $y_{CH4} = 0.20$ and $y_{CO2} = 0.80$, and the upper stream boundary condition as $y_{CO2} = 1.0$. Two 3D diagrams of CH_4 and CO_2 variations within the coal matrix are shown in Figures 10a, b, respectively, for 1 h of operation. From these two figures, it can be seen that even after 1 h, there is still a long way to go to complete the CO_2 sequestration process. In addition to slow dynamics, another notable feature of the concentration within the coal matrix is the high non-uniformity. There are tremendous differences between the concentrations in the upstream and downstream halves of the specimen. This implies that the hybrid distributed-lumped parameter model using averaged properties within the coal matrix suggested by Gilman and Beckie[10] may lead to significant errors without adjustments of model parameters. Although we are unable to measure the concentration profiles inside coal specimens at this stage, the predicted time scales agree with the overall measurement data very well.

Simulations for longer operating times were carried out, which provide additional physical insights to the process. Mole fraction surfaces of CH_4 and CO_2 in the coal matrix for 2 h operation are depicted in Figures 11a, b, respectively. Note that at the down stream boundary, the mole fraction of CH_4 does not decrease monotonically with time. It increases first followed by a gradual decrease. A consistent trend can be observed for CO_2 trajectory in the opposite direction, decreasing initially, followed by a gradual increase. This phenomenon has also been observed in our laboratory. The existence of an interior maximum or minimum point is normally caused by two opposing factors. It can be shown that the gas phase diffusion and viscous flow within macro- and

Table 2. Default Values in Adsorption-Diffusion Model

Gas Property	CH_4		CO_2
Compressibility factor	0.95		0.76
Self diffusivity D_s (m^2/sec)	3.51×10^{-8}		4.65×10^{-9}
Surface diffusivity D_μ (m^2/sec)	3.31×10^{-12}		1.60×10^{-13}
Knudsen diffusivity in Meso-pores D_K (m^2/sec)	6.27×10^{-6}		3.79×10^{-6}
Binary diffusivity D_{AB} for CH_4—CO_2 (m^2/sec)		$4.81–7.87 \times 10^{-6}$	
Saturated adsorption concentration $C_{\mu s}$ (mol/m^3)	2.44×10^3		2.12×10^3
Langmuir parameter b (MPa^{-1})	0.27		1.45
Parameter η in Langmuir–Freundlich equation	0.89–1.0		0.91–1.0
Mean-size adsorption Energy E($\langle w \rangle$) (J/mol)	1.30×10^4		1.80×10^4
Pore Property	**Micro-Pores**	**Meso-Pores**	**Macro-Pores**
Half-width w (m)	4.5×10^{-10}	6.5×10^{-9}	4.0×10^{-8}
Porosity ε	0.13	0.01	0.02
Pore size distribution f(w)	Lognormal or Γ	Lognormal	
α in $\varepsilon/\tau = \varepsilon^\alpha$ (Eqn. 5)		1.4	1.4

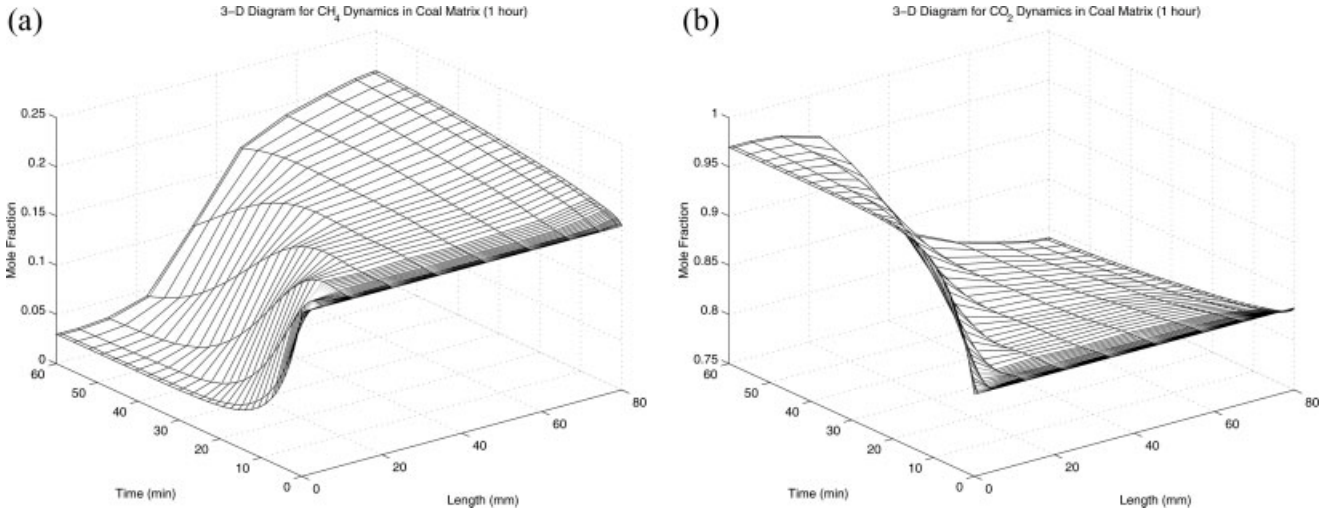

Figure 10. (a) Three-dimensional diagram for CH_4 Dynamics in coal matrix (1 h operation); (b) three-dimensional diagram for CO_2 dynamics in coal matrix (1 h operation).

meso-pores due to partial pressure gradients promote z-direction transport of CO_2. On the other hand, because of different affinities to graphite walls possessed by CH_4 and CO_2 "counter-adsorption diffusion" can be observed in micro-pores. The counter-adsorption diffusion prevents the fast transport of CO_2 along the z-direction because of the replacement of the adsorbed CH_4 by CO_2 in micro-pores, leading to the slowed down dynamics of CO_2 transport. As an overall result of these two opposing factors, the dynamic trajectories with interior extreme points at the down-stream boundary, as shown in Figure 11, are developed.

Two 3D diagrams for the variations of CH_4 and CO_2 fluxes in coal matrix for the 2 h operation are shown in Figures 12a, b, respectively. The much higher CO_2 flow rate shown in the figures was clearly due to the inlet boundary conditions, in which CO_2 and CH_4 mole fractions were 1 and 0, respectively. The two figures also show that CH_4 flow rate increases along the z-direction, whereas CO_2 flow rate changes in the opposite direction. This verifies the counter-sorption theory. Because of the relatively higher adsorption affinity of CO_2, CH_4 molecules originally adsorbed on the coal surface were gradually replaced by CO_2, leading to the adsorption of CO_2 and de-sorption of CH_4. The simulation results for various molar fluxes can be well explained physically, providing an improved insight into the counter-sorption phenomena.

The fractional uptake for species i at time t is defined as:

$$fr_i(t) = \frac{\left[\varepsilon_t \overline{C}_i(t) + (1-\varepsilon_t)\left\langle \overline{C}_{\mu i}(t)\right\rangle_e\right] - \left[\varepsilon_t \overline{C}_i(0) + (1-\varepsilon_t)\left\langle \overline{C}_{\mu i}(0)\right\rangle_e\right]}{\left[\varepsilon_t \overline{C}_i(t_f) + (1-\varepsilon_t)\left\langle \overline{C}_{\mu i}(t_f)\right\rangle_e\right] - \left[\varepsilon_t \overline{C}_i(0) + (1-\varepsilon_t)\left\langle \overline{C}_{\mu i}(0)\right\rangle_e\right]} \tag{49}$$

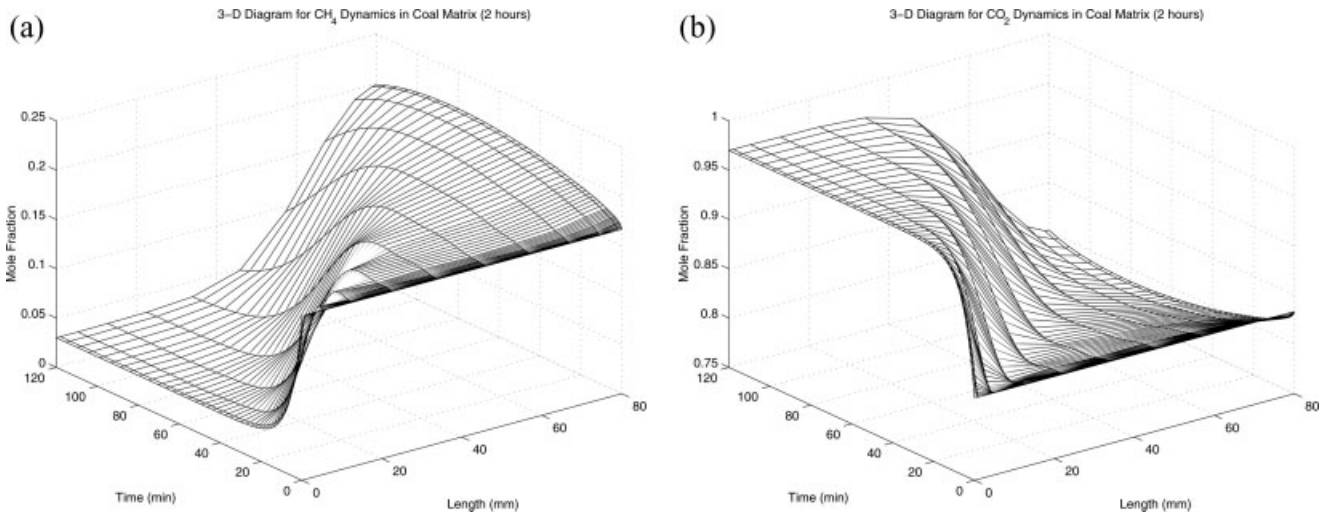

Figure 11. (a) Three-dimensional diagram for CH_4 dynamics in coal matrix (2 h operation); (b) three-dimensional diagram for CO_2 dynamics in coal matrix (2 h operation).

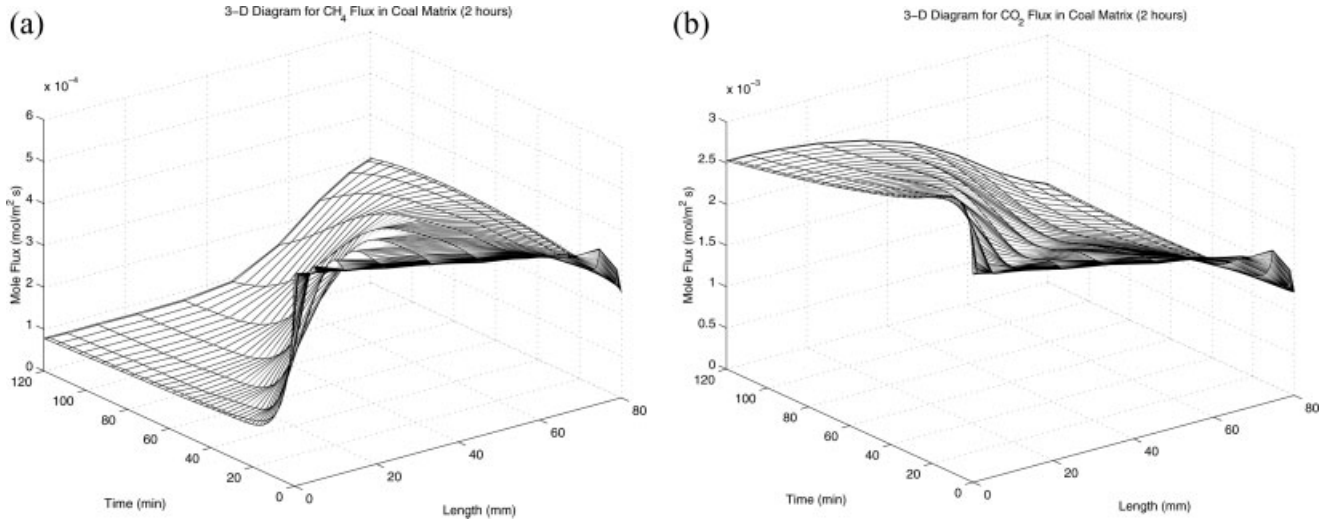

Figure 12. (a) Three-dimensional diagram for CH_4 flux in coal matrix (2 h operation); (b) three-dimensional diagram for CO_2 flux in coal matrix (2 h operation).

for adsorption and

$$fr_i(t) = \frac{\left[\varepsilon_t \overline{C}_i(t_f) + (1-\varepsilon_t)\langle \overline{C}_{\mu i}(t_f)\rangle_e\right] - \left[\varepsilon_t \overline{C}_i(t) + (1-\varepsilon_t)\langle \overline{C}_{\mu i}(t)\rangle_e\right]}{\left[\varepsilon_t \overline{C}_i(t_f) + (1-\varepsilon_t)\langle \overline{C}_{\mu i}(t_f)\rangle_e\right] - \left[\varepsilon_t \overline{C}_i(0) + (1-\varepsilon_t)\langle \overline{C}_{\mu i}(0)\rangle_e\right]} \quad (50)$$

for de-sorption. In Eqs. 49 and 50, t_f stands for the final time of operation, $\overline{C}$ and $\overline{C}_\mu$ are the spatially averaged concentrations in the gas phase and adsorbed phase, respectively. The fractional uptakes for CH_4 and CO_2 are depicted in Figure 13. The curves show nearly linear fractional uptake dynamics in the specified operational range. From Eqs. 49 and 50, it can be seen that the fractional uptakes should be bounded by $0 \leq fr \leq 1$. However, Figure 13 shows that at early de-sorption stage, fr may slightly greater than 1 for CH_4. This is caused by numerical oscillations near the discontinuous points of the boundary conditions, also known as the Gibbs phenomenon.[39]

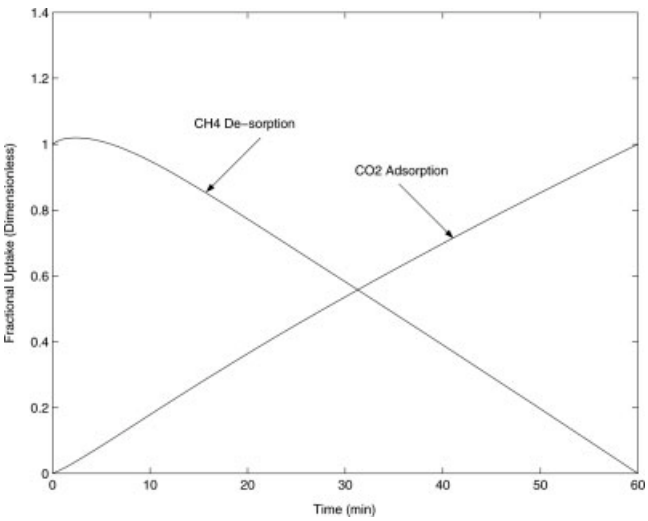

Figure 13. CH_4 and CO_2 uptake dynamics.

Significance of pore size distributions

Compared with models based on mean pore sizes, the incorporation of pore size distributions into dynamic models described in the previous section may lead to about 10 times longer computing times. It is therefore important to analyze the necessity to adopt the pore size dependent methods. A comparative study is carried out between the simplified approach using the mean micro-pore size and the effective averaging strategy based on distribution density functions. Selected computational results are shown in Table 3. It can be shown that both approaches provide similar results for the adsorption energy, E, and the adsorbed phase concentrations, C_μ. However, tremendous differences are identified in computations of Langmuir parameters b_i for both gases, and the surface diffusivity D_μ for CO_2. This is because that both b

Table 3. Values Based on Mean Micro-Pore Size and Size Distributions

Property	CH_4	CO_2
$C_\mu(\langle w\rangle)$ (mol/m^3)	49.3	7.36×10^2
$\langle C_\mu(w)\rangle$ (mol/m^3)	47.1	6.92×10^2
$(C_\mu(\langle w\rangle)-\langle C_\mu(w)\rangle)/\langle C_\mu(w)\rangle \times 100\%$	4.8%	6.4%
$E(\langle w\rangle)$ (J/mol)	1.30×10^4	1.80×10^4
$\langle E(w)\rangle$ (J/mol)	1.32×10^4	1.75×10^4
$(E(\langle w\rangle)-\langle E(w)\rangle)/\langle E(w)\rangle \times 100\%$	−1.5%	2.8%
$b(\langle w\rangle)$ (mol/m^3)$^{-1}$	6.36×10^{-4}	2.73×10^{-3}
$\langle b(w)\rangle$ (mol/m^3)$^{-1}$	2.13×10^{-3}	1.83×10^{-2}
$(b(\langle w\rangle)-\langle b(w)\rangle)/\langle b(w)\rangle \times 100\%$	−70.1%	−85.1%
$\mathrm{Max}\{b\}/b(\langle w\rangle)$	25.2	37.8
$D_\mu(\langle w\rangle)$ (m^2/sec)	3.32×10^{-12}	1.60×10^{-13}
$\langle D_\mu(w)\rangle$ (m^2/sec)	3.30×10^{-12}	2.03×10^{-13}
$(D_\mu(\langle w\rangle)-\langle D_\mu(w)\rangle)/\langle D_\mu(w)\rangle \times 100\%$	0.6%	−26.9%

and D_μ are exponential functions of E as shown in Eqs. 27 and 29, respectively, and E is very sensitive to micro-pore sizes as depicted in Figure 4. It can also be seen from Table 3 that the ratios of Maximum {b} over b($\langle w \rangle$) for both CH_4 and CO_2 are very large. Consequently, it can be concluded that if a significant amount of micro-pores lies within the size range from 3.2 to 4.2 Å correlated to the peaks of the adsorption energy curves, any simplified methods based on mean sizes could lead to unacceptable errors.

It is interesting to note that although the pair {b($\langle w \rangle$), $\langle b(w) \rangle$} are very different from each other, $C_\mu(\langle w \rangle)$ and $\langle C_\mu(w) \rangle$ are reasonably close to each other. This is because the processes are operated under a high pressure (400 kPa), leading to error cancellation when the Langmuir isotherm given by Eq. 30 is applied. However, in low pressure operations, unacceptable inconsistency will be observed for C_μ computations using different approaches. Under any pressures, the pair {$D_\mu(\langle w \rangle)$, $\langle D_\mu(w) \rangle$} are very different. The necessity for the incorporation of pore size dependent computations can be justified on this basis.

Prospective industrial applications of the integrated model

The integrated modeling framework has far reaching implications in industrial applications. A few application examples are listed as follows.

1. Prediction of the dynamic behavior of CO_2 sequestration processes.
2. Improved process design through the determination of optimal operational conditions.
3. Optimal control for accelerated methane residual recovery.[40]
4. Process diagnosis through identifying likely causes for quality problems and process deviations.

Conclusion and Recommendation

Through comprehensive simulation and experimental studies, the following conclusions can be drawn.

1. An integrated modeling approach to the dynamics of mass transfer in porous media with particular applications to CO_2 sequestration in coal seams is developed in this work. The process under study can be depicted by a spectrum of representations ranging between a very simple black-box model based on input-output data only, and a highly complex mechanistic model consisting of several sub-models described by a large scale partial differential equation (PDE) system with adequate parameter identification techniques. The development of an upper-middle class model is described in detail in this paper. The model is represented by a system of matrix partial differential equations incorporating the Stefan-Maxwell analysis, online computations of physical properties, determination of pore size dependent parameters, and the EST-SFA procedure.
2. The overall model integrates key sub-processes represented by a number of sub-models. These include fluid flow in cleats, dynamic coal permeability-dimension variations induced by gas adsorption, fluid flow and diffusion in macro- and meso-pores, adsorption and surface diffusion within micro-pores. Furthermore, parameter estimation is done through thermodynamic computations, molecular simulations, and online identification. Most important parameters are computed using well established equations with a minimum of empirical curve-fitting. Consequently, the overall model, which has been constructed from literature based sub-models, provides a more complete and flexible representation.
3. Three main mechanisms of coal swelling and pore size changes during adsorption and de-sorption processes are analyzed through molecular simulations and thermodynamic computations. We speculate that the adsorption induced C—C bond extension is responsible for the dimensional changes of the basal planes, which could be the dominant mechanism for permeability variations, and the interactions between adsorbate and adsorbent molecules are the driving forces leading to the dimensional variations of the edge-site planes. Notable C-metal distance changes during adsorption/de-sorption processes may lead to dimensional variations of both basal and edge-site planes.
4. The macroscopic level model is validated using a true triaxial stress coal permeameter (TTSCP), which provides accurate dynamic measurements of gas flow-rates, compositions, temperatures and pressures in three orthogonal directions.
5. Misleading results could be obtained using the mean size based approximations for micro-pores due to highly nonlinear characteristics of the functions connecting pore size with adsorption energy, adsorption energy with Langmuir parameters, and adsorption energy with surface diffusivity. Consequently, the simplified methods based on mean micro-pore sizes must be used with caution.

The following comments summarize the key challenges in the ECBM modeling areas, which are recommended for future work.

1. The deep coal seams available for CO_2 sequestration are normally below the water table. Consequently, studies on multiphase flow and effects of moisture contents on gas adsorption characteristics should be given high priority in the future work.
2. The 2D and 3D integrated models should be developed based on the current multiple 1D model. Limitations of the effective diffusivity based methods can hopefully be eliminated.
3. The issue of variations of adsorption characteristics with external stress changes has not been adequately addressed in the literature, which requires further research efforts.
4. A number of model parameters cannot be determined rigorously. These mainly include the surface diffusivities D_μ, tortuosities of various pore types, and adsorption parameters b_i and β. More accurate estimations could be possible through molecular simulations and advanced experimental investigations.
5. An experimental validation of the 3D concentration surfaces within coal matrices shown in Figures 10 and 11 is yet to be performed using a modified design of TTSCP.
6. Micro-pore size distributions affect adsorption and surface diffusion processes significantly as shown in Table 3. Unfortunately, commonly accepted methods for the accurate measurement of micro-pore size distributions have not appeared in the literature. Further work along this line will certainly lead to the improved understanding of the transport phenomena in micro-pores.

7. Permeability measurement data show substantial scale differences between 40 mm cube sub-samples and a parent 80 mm cube specimen, due mainly to the higher probability of cleats being truncated and dead-ending into specimen holder side walls, for small sample sizes. This implies that the experimental results using small specimens may not represent the real permeability of large scale coal seams. It is necessary to confirm that 80 mm cube samples are adequately representative of bulk seam properties. From a practical perspective 80 mm samples are the largest that can be obtained from the largest cylindrical 146 mm cores.

Notation

a = aperture of slit fractures, m; ratio of activation energy to adsorption energy, dimensionless
a_i-a_n = parameters in ARX model
A = cross section area of coal specimen, m^2
$\mathbf{A}$ = collocation matrix, dimensionless
b = parameter in Langmuir or Langmuir-Freundlich isotherm, m^3/mol
b_i-b_n = parameters in ARX model
B = macro- and meso-pore permeability, m^2
$\mathbf{B}$ = Stefan-Maxwell matrix, s/m^2
C_i = gas phase concentration for species i, mol/m^3
$\mathbf{C}$ = vector of gas phase concentration, mol/m^3
D = diffusivity, m^2/s
$\mathbf{D}$ = diffusivity matrix, m^2/s
e = error in ARX model
E = adsorption energy, J/mol
E = Young's modulus, MPa
f = probability density function
fr = fractional uptake, dimensionless
g = gravitational acceleration, m/s^2
h = cleat spacing, m
$\mathbf{I}$ = identity matrix
$\mathbf{IB}$ = inverse of matrix $\mathbf{B}$, m^2/s
J_{μ_i} = molar flux in micro-pores for species i, $mol/(m^2\ s)$
$\mathbf{J}_\mu$ = vector of molar flux in micro-pores, $mol/(m^2\ s)$
K = permeability, m^2
k_{ads} = adsorption rate constant, $s^{-1}/(N/m^2)$
k_{des} = de-sorption rate constant, $s^{-1}/(N/m^2)$
L = length of coal specimen, m
m_i = block-to-fracture mass cross flow rate for species i, $mol/(m^2\ s)$
$\mathbf{m}$ = vector of block-to-fracture mass cross flow rate, $mol/(m^2\ s)$
M = molecular weight, kg/mol
$\mathbf{M}$ = mass matrix for matrix representation of differential algebraic equations
N_i = molar flux for species i, $mol/(m^2\ s)$
$\mathbf{N}$ = vector of molar flux, $mol/(m^2\ s)$
NC = number of component, dimensionless
p_b = bulk pressure, N/m^2
p_s = solvation pressure, N/m^2
P = total pressure, N/m^2
P_i = partial pressure for species i, N/m^2
$\mathbf{P}$ = vector of partial pressure, N/m^2,
Q = volumetric gas flow rate, m^3/s
Q_i = function defined in Eq. 18, m/s
R = ideal gas constant, J/(K mol)
ΔS = change of adsorbed mass, kg/m^3
t = time variable, s
T = temperature, K
u = input variable in ARX model
ΔU = relative volume change per unit volume of specimen, m^3/m^3
V = gas velocity, m/s
w = half-width of slit pore, m
x = spatial coordinates, m
y = mole fraction, dimensionless; output variable in ARX model
z = spatial coordinates, m
Z = compression factor, dimensionless

Greek letters

α = parameter in Archie's law, dimensionless
β = adsorption affinity of adsorbent, $(K\ kg/mol)^{1/2}/\ (mol/m^3)$
γ = volumetric swelling coefficient, m^3/kg
ε = porosity, dimensionless
ζ = dimensionless spatial variable defined in [0, 1]
η = parameter in Langmuir–Freundlich isotherm, dimensionless
λ = half distance between two fractures, m
Λ = diagonal matrix defined by Eq. 23, s/m^2
μ = viscosity, $(N\ s)/m^2$
ν = Poison ratio, dimensionless
Π = pressure acting between micro-pore walls, N/m^2
ρ = gas density, kg/m^3
τ = tortuosity, dimensionless
ψ = correction parameter in Darcy's law, dimensionless

Subscripts

c = coal matrix; convection; critical value
d = diffusion
e = effective
f = fracture
hy = hypothetic
i = species i
ij = binary pair i-j
K = Knudsen diffusion
m = mean value; gas mixture
ma = macro-pore
me = meso-pore
r = reduced property
t = total value
μ = micro-pore
μs = adsorption saturation

Superscript

E-F = effective medium theory with the smooth field approximation
s = geometric factor

Mathematical symbols

$\langle\bullet\rangle$ = arithmetic average
$\langle\bullet\rangle_e$ = effective average

Literature Cited

1. Tsotsis TT, Patel H, Najafi BF, Racherla D, Knackstedt MA, Sahimi M. Overview of laboratory and modelling studies of carbon dioxide sequestration in coal beds. *Ind Eng Chem Res.* 2004;43:2887–2901.
2. White CM, Smith DH, Jones KL, Goodman AL, Jikich SA, LaCount RB, DuBose SB, Ozdemir E, Morsi BI, Schroeder KT. Sequestration of carbon dioxide in coal with enhanced coal-bed methane recovery—A review. *Energy Fuels.* 2005;19:659–724.
3. Box GEP, Draper NR. *Empirical Model-Building and Response Surfaces*. New York: Wiley, 1987.
4. Clarkson CR, Bustin RM. The effect of pore structure and gas pressure upon the transport properties of coal: a laboratory and modelling study. II. Adsorption rate modelling. *Fuel.* 1999;78:1345–1362.
5. Shi JQ, Durucan S. A bidisperse pore diffusion model for methane displacement desorption in coal by CO_2 injection. *Fuel.* 2003;82:1219–1229.
6. Yang RT. *Gas Separation by Adsorption Processes*. London:Imperial College Press, 1997.
7. Jakubov TS, Mainwaring DE. Adsorption-induced dimensional changes of solids. *Phys Chem Chem Phys.* 2002;4:5678–5682.
8. Ustinov EA, Do DD. Effect of adsorption deformation on thermodynamic characteristics of a fluid in slit pores at sub-critical conditions. *Carbon.* 2006;44:2652–2663.
9. Cui XJ, Bustin RM, Dipple G. Selective transport of CO_2, CH_4 and N_2 in coals: insights from modelling of experimental gas adsorption data. *Fuel.* 2004;83:293–303.
10. Gilman A, Beckie R. Flow of coal-bed methane to a gallery. *Transport Porous Media.* 2000;41:1–16.

11. Krishna R, Wesselingh JA. The Maxwell-Stefan approach to mass transfer. *Chem Eng Sci*. 1997;52:861–911.
12. Jackson R. *Transport in Porous Catalysts*. Amsterdam: Elsevier, 1977.
13. Wang FY, Bhatia SK. A generalised dynamic model for char particle gasification with structure evolution and peripheral fragmentation. *Chem Eng Sci*. 2001;56:51–65.
14. Krishna R, van Baten JM. Diffusion of alkane mixtures in zeolites: validating the Maxwell-Stefan formulation using MD simulations. *J Phys Chem B*. 2005;109:6386–6396.
15. Krishna R, van Baten JM. Describing binary mixture diffusion in carbon nanotubes with the Maxwell-Stefan equations. An investigation using molecular dynamics simulations. *Ind Eng Chem Res*. 2006;45:2084–2093.
16. Wang K, Do DD. Multicomponent adsorption, desorption and displacement kinetics of hydrocarbon on activated carbon—dual diffusion and finite kinetic model. *Separ Purif Technol*. 1999;17:131–146.
17. Massarotto P. 4-D coal permeability under true triaxial stresses and constant volume conditions. PhD thesis, The University of Queensland, Australia, 2002.
18. Steele WA. *The Interaction of Gases with Solid Surface*. Oxford: Pergamon, 1974.
19. Gamson PD, Beamish BB, Johnson DP. Coal microstructure and micropermeability and their effects on natural gas recovery. *Fuel*. 1993;72:87–99.
20. Levine JR, *Coalification: The evolution of coal as source rock for oil and gas*. In AAPG Studies in Geology No. 38 ''Hydrocarbons for Coal,'' edited by Law BE and Rice DD, pp 39–77. Tulsa, OK: American Association of Petroleum Geologists. (ISBN 0-89181-046-3).
21. Do DD, Wang K. A new model for the description of adsorption kinetics in heterogeneous activated carbon. *Carbon*. 1998;36:1539–1554.
22. Sahimi M. *Flow and transport in porous media and fractured rock: from classical methods to modern approaches*. Weinheim: VCH, 1995.
23. Do DD, Do HD. Non-isothermal effects on adsorption kinetics of hydrocarbon mixture in activated carbon. *Separ Purif Technol*. 2000;20:49–65.
24. Sotirchos SV. Multicomponent diffusion and convection in capillary structures. *AIChE J*. 1989;35:1953–1961.
25. Sotirchos SV, Burganos VN. Analysis of multicomponent diffusion in pore networks. *AIChE J*. 1988;34:1106–1118.
26. Adler PM. *Porous media: geometry and transport*. Boston: Butterworth-Heinemann, 1992.
27. Van Krevelen DW. Coal: typology-physics–chemistry-constitution, 3rd edition. Amsterdam: Elsevier, 1993.
28. Palmer ID, Mansoori J. How permeability depends on stress and pore pressure in coal-beds: a new model. *SPE Reservoir Eval Eng*. 1998;1:539–544.
29. Zhu ZH, Lu GQ, Wang FY. Why H atom prefer the on-top site and alkali metals favour the middle hollow site on the basal plane of graphite. *J Phys Chem B*. 2005;109:7923–7927.
30. Zhang Y, Toebes ML, van der Eerden A, O'Grady WE, de Jong KP, Koningsberger DC. Metal particle size and structure of the metal-support interface of carbon-supported platinum catalysts as determined with EXAFS spectroscopy. *J Phys Chem B*. 2004;108:18509–18519.
31. Zhu ZH, Lu GQ. Comparative study of Li, Na, and K adsorptions on graphite by using ab initio method. *Langmuir*. 2004;20:10751–10755.
32. Reid RC, Prausnitz JM, Poling BE. *The Properties of Gases and Liquids*, 4th edition. New York: McGraw-Hill, 1987.
33. Bhatia SK, Nicholson D. Hydrodynamic origin of diffusion in nanopores. *Phys Rev Lett*. 2003;90:016150-1-016150-4.
34. Mathur GP, Thodos G. The self-diffusivity of substances in the gaseous and liquid states. *AIChE J*. 1965;11:613–616.
35. Finlayson BA. *The Method of Weighted Residuals and Variational Principles: With Applications in Fluid Mechanics, Heat and Mass Transfer*. New York: Academic Press, 1972.
36. Villadsen J, Michelsen ML. *Solution of Differential Equation Models by Polynomial Approximation*. Englewood Cliffs, New Jersey: Prentice-Hall, 1978.
37. Finlayson BA. *Numerical Methods for Problems with Moving Fronts*. Seattle: Ravenna Park, 1992.
38. Ljung L. *System Identification: Theory for the User*. Upper Saddle River, New Jersey: Prentice-Hall, 1987.
39. Kreyszig E. *Advanced Engineering Mathematics*, 4th edition. New York: Wiley, 1999.
40. Wang FY, Zhu ZH, Massarotto P, Rudolph V. A simplified dynamic model for accelerated methane residual recovery from deep coals. *Chem Eng Sci*. Submitted for publication.

Appendix A: Steele 10-4-3 Potential Energy Equation

The Steele 10-4-3 potential energy equation[18] is given by:

$$\Phi(z,w) = \frac{5}{3}\Phi_0\left\{\frac{2}{5}\left[\frac{\sigma_{sg}^{10}}{(w+z)^{10}} + \frac{\sigma_{sg}^{10}}{(w-z)^{10}}\right] - \left[\frac{\sigma_{sg}^{4}}{(w+z)^{4}} + \frac{\sigma_{sg}^{4}}{(w-z)^{4}}\right] - \left[\frac{\sigma_{sg}^{4}}{3\Delta(0.61\Delta+w+z)^{3}} + \frac{\sigma_{sg}^{4}}{3\Delta(0.61\Delta+w-z)^{3}}\right]\right\}$$

$$\Phi_0 = \frac{6}{5}\pi\rho_s\varepsilon_{sg}\sigma_{sg}^2\Delta \qquad \text{(A1)}$$

In Eq. A1, z is the distance from the central plane of the pore, w is the half width of slit-shaped pores, Φ_0 is the minimum interaction energy between a gas molecule and a single lattice layer of the adsorbent, ρ_s is the number of lattice molecules per unit volume, Δ is the spacing of lattice layers, ε_{sg} and σ_{sg} are the cross potential well depth and the effective diameter for the adsorbate-adsorbent molecule atoms. These cross parameters are calculated using the Lorentz-Berthelot rules as follows: $\varepsilon_{sg} = (\varepsilon_s\varepsilon_g)^{1/2}$, and $\sigma_{sg} = (\sigma_s + \sigma_g)/2$. The pair ($\varepsilon_s$, σ_s) and (ε_g, σ_g) are the Lennard-Jones parameters for a surface atom and a gas molecule, respectively.

Appendix B: Lognormal and Γ-Distribution Functions

The general representation of the lognormal distribution is given by:

$$f(w) = \frac{1}{w\sigma(2\pi)^{1/2}}\exp\left\{\frac{-[\log(w/m)]^2}{2\sigma^2}\right\} \qquad \text{(B1)}$$

where f is the probability density function, also known as the distribution function, the parameters m and σ are median and standard deviation, respectively. The computed distribution function with $\sigma = 0.6$ and $m = 65$ Å is very close to the measured one for meso-pores in a number of coal specimens.

The general representation of a Γ-distribution is described as:

$$f(w) = \frac{(w/b)^{c-1}[\exp(-w/b)]}{b\Gamma(c)}$$

$$\Gamma(c) = \int_0^\infty \exp(-u)\,u^{c-1}du \qquad \text{(B2)}$$

where b and c are denoted as the scale and shape parameters, respectively. The lognormal and Γ distributions for micro-

pores in coal specimens with $\sigma = 0.6$, $m = 4.5$ Å, $c = 2$, and $b = 1$ are reasonably close to the measured distributions.

Appendix C: Gilman and Beckie Permeability Model

The Gilman and Beckie[10] permeability model is described as:

$$\frac{\Delta K}{K} = \frac{3v}{(1-v)}\frac{\Delta P_f}{E_f} - \frac{3\gamma E}{(1-v)}\frac{\Delta S}{E_f} \tag{C1}$$

Based on Eq. C1, they developed a constitutive equation for permeability represented as follows:

$$K = K_0 \exp\left(\frac{3v}{(1-v)}\frac{\Delta P_f}{E_f}\right) \exp\left(-\frac{3\gamma E}{(1-v)}\frac{\Delta S}{E_f}\right) \tag{C2}$$

In Eqs. C1 and C2, K_0 is the initial permeability, and ΔP_f is the pressure variation in fractures.

Appendix D: Derivation of Eq. 26

The adsorption rate $r_{a,i}$ and de-sorption rate $r_{d,i}$ are described by:

$$r_{a,i} = k_{ads,i} C_i^{\eta_i}\left[C_{\mu s,i} - \sum_{j=1}^{NC} C_{\mu,j}\right]$$
$$r_{d,i} = k_{des,i} C_{\mu,i} \tag{D1}$$

Equation D1 is the modified format of the equation originally proposed by Wang and Do[16] through the incorporation of the parameter η_i. At equilibrium, the following equation can be obtained from Eq. 6:

$$C_i^{\eta_i} = \frac{C_{\mu,i}}{b_i\left[C_{\mu s,i} - \sum_{j=1}^{NC} C_{\mu,j}\right]}$$
$$b_i = k_{ads,i}/k_{des,i} \tag{D2}$$

From Eq. D2, we directly obtain:

$$C_{hy,i} = \left[\frac{1}{b_i}\frac{C_{\mu,i}}{C_{\mu s,i} - \sum_{j=1}^{NC} C_{\mu,j}}\right]^{1/\eta_i} \tag{D3}$$

Since b_i is a constant, after combining b_i with $1/\eta_i$ for notational simplicity, Eq. 26 is developed.

Appendix E: Computations of Physical Properties

The main physical properties of gases are estimated using methods and working equations recommended and detailed in Reid et al.[32] Diffusion coefficients for binary gas systems at low to moderate pressures are predicted using a working equation based on the Chapman-Enskog theory[32] [Ref. 32, p. 582, Eqs. (11-3.2)]. The pure gas viscosities with effects of intermolecular forces are computed by incorporating the Lennard–Jones potential function into the Chapman-Enskog equation[32] [Ref. 32, pp. 392–393, Eqs. (9-3.9) and (9-4.3)], while the Wilke method[32] is used for the determination of viscosities of gas mixture [Ref. 32, p. 407, Eqs. (9-5.13)–(9-5.15]

Since the processes operate under high pressures, it is necessary to account for the effects of pressure on physical properties. The diffusivity variations with pressures can be quantified by using the Takahashi correlation[32] [Ref. 32, p. 592, Eqs. (11-5.1)–(11-5.5)], showing non-trivial pressure effect. For the pressure range in our studies (5.0–70.0 bar), the error could be up to 30% using the popular correlations for low to moderate pressures without corrections. The viscosity of a gas is a strong function of pressure near the critical point and at reduced temperature of about 1 to 2 at high pressures. Since the critical values for CO_2 are: $T_c = 304.1$ K and $P_c = 73.8$ bar, dramatic viscosity changes could happen to CO_2 rich mixtures. However, most of our experiments are carried out below 50 bar, the pressure effect on gas viscosities can be ignored for the moment.

There is no rigorous method for the computations of surface diffusivities without carrying out molecular simulations for idealized systems.[33] However, it is noteworthy that the surface diffusivity in a cylindrical pore without accounting for the effects of porosity and tortuosity is in the same order of magnitude as the self diffusivity (10^{-9}–10^{-8} m^2/sec). Consequently, self diffusivities can be used as the starting point for the estimation of $D^0_{\mu\infty}$. A simple method for the computation of the self diffusivity developed Mathur and Thodos[34] is given by:

$$D_s = 3.67 \times 10^{-5}\frac{T_c^{5/6} T_r^{3.5}}{M^{1/2} P_c^{2/3} P_r^{0.10}} \tag{E1}$$

This approximation will be replaced by more rigorous computations in the future.

Manuscript received Sept. 1, 2006, and revision received Dec. 27, 2006.